Cell Reports

CellPress
OPEN ACCESS

Article

Elevation of hilar mossy cell activity suppresses hippocampal excitability and avoidance behavior

Kai-Yi Wang,[1] Jei-Wei Wu,[1] Jen-Kun Cheng,[3,4] Chun-Chung Chen,[5] Wai-Yi Wong,[1] Robert G. Averkin,[6] Gábor Tamás,[6] Kazu Nakazawa,[7,8] and Cheng-Chang Lien[1,2,9,*]

[1]Institute of Neuroscience, National Yang Ming Chiao Tung University, Taipei 11221, Taiwan
[2]Brain Research Center, National Yang Ming Chiao Tung University, Taipei 11221, Taiwan
[3]Department of Medicine, Mackay Medical College, New Taipei 252, Taiwan
[4]Department of Anesthesiology, Mackay Memorial Hospital, Taipei 104, Taiwan
[5]Institute of Physics, Academia Sinica, Taipei 115, Taiwan
[6]ELKH-SZTE Research Group for Cortical Microcircuits, Department of Physiology, Anatomy and Neuroscience, University of Szeged, Közép fasor 52, Szeged 6726, Hungary
[7]Department of Neuroscience, Southern Research, Birmingham, AL 35205, USA
[8]Department of Neurobiology, University of Alabama at Birmingham, Birmingham, AL 35294, USA
[9]Lead contact
*Correspondence: cclien@nycu.edu.tw
https://doi.org/10.1016/j.celrep.2021.109702

SUMMARY

Modulation of hippocampal dentate gyrus (DG) excitability regulates anxiety. In the DG, glutamatergic mossy cells (MCs) receive the excitatory drive from principal granule cells (GCs) and mediate the feedback excitation and inhibition of GCs. However, the circuit mechanism by which MCs regulate anxiety-related information routing through hippocampal circuits remains unclear. Moreover, the correlation between MC activity and anxiety states is unclear. In this study, we first demonstrate, by means of calcium fiber photometry, that MC activity in the ventral hippocampus (vHPC) of mice increases while they explore anxiogenic environments. Next, juxtacellular recordings reveal that optogenetic activation of MCs preferentially recruits GABAergic neurons, thereby suppressing GCs and ventral CA1 neurons. Finally, chemogenetic excitation of MCs in the vHPC reduces avoidance behaviors in both healthy and anxious mice. These results not only indicate an anxiolytic role of MCs but also suggest that MCs may be a potential therapeutic target for anxiety disorders.

INTRODUCTION

Anxiety disorders are associated with the dysfunction of γ-aminobutyric acid (GABA)-ergic transmission and altered neuronal activity in the hippocampal subfields (Dong et al., 2020; Engin et al., 2016; Schoenfeld et al., 2013). Compared to its dorsal counterpart, the ventral hippocampus (vHPC) has been linked to affective and motivated behaviors because of its connections with several limbic structures (Bannerman et al., 2003; Barkus et al., 2010; Ciocchi et al., 2015; Fanselow and Dong, 2010; Weeden et al., 2015). Multimodal sensory information from the cortex is mainly transmitted to the first station of the HPC, the dentate gyrus (DG) (Amaral et al., 2007; Lisman, 1999; Squire, 2009). Increased DG excitability is associated with a higher susceptibility to stress-induced anxiety disorders. Conversely, attenuated DG excitability of the vHPC confers stress resilience (Anacker et al., 2018). Selective deletion of α2-containing $GABA_A$ receptors in the DG results in increased anxiety (Engin et al., 2016). Information mainly flows from the DG to the CA1 output neurons via the trisynaptic pathway. More recently, CA1 neurons in the vHPC are shown to encode anxiety-related information (Ciocchi et al., 2015; Jimenez et al., 2018; Padilla-Coreano et al., 2016). Furthermore, increasing the activity of CA1 output neurons enhances avoidance of aversive contexts (or aversive behavior), whereas decreasing them disrupts avoidance behavior (Jimenez et al., 2018; Padilla-Coreano et al., 2016).

In addition to extrinsic inputs, DG cells participate in the regulation of DG activity. The DG consists of glutamatergic principal neurons and GABAergic interneurons (INs). Granule cells (GCs) constitute the vast majority of principal neurons in the DG and project to the downstream CA3 region. The excitation/inhibition balance in GCs is critical to cognitive processes, such as pattern separation and mood regulation (Burghardt et al., 2012; Christian et al., 2014; Deng et al., 2010; Kheirbek and Hen, 2011). Several types of local GABAergic INs mediate feedforward and feedback inhibition, thereby regulating the dynamics of GCs (Anacker and Hen, 2017; Lee et al., 2016; Liu et al., 2014a; Schoenfeld et al., 2013; Zou et al., 2016). In addition to GCs, mossy cells (MCs) in the polymorphic hilar region of the DG are another major type of glutamatergic principal neuron present in the DG. MCs receive their main excitatory inputs from GCs (Amaral, 1978; Williams et al., 2007) and send extensive divergent projections to GCs and local INs along the longitudinal axis of the hippocampus (Scharfman, 1995, 2016; Scharfman and Myers, 2013). MC

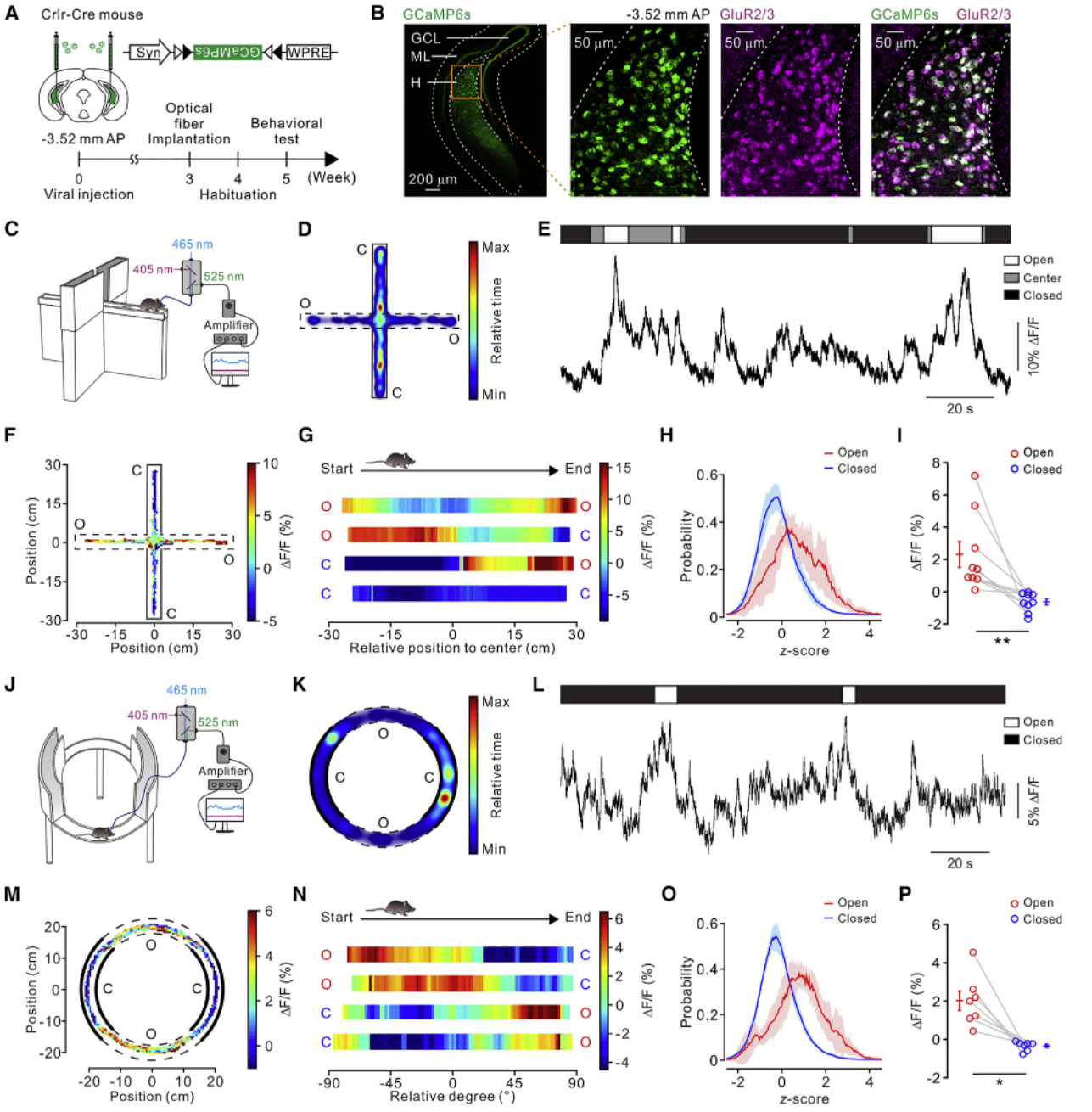

Figure 1. Increased MC activity during open-arm exploration

(A) Experimental schematic and timeline.

(B) Left, virally expressed GCaMP6s in the DG; scale bar, 200 μm. Center, higher magnification of the GCaMP6s-expressing cells (green) and GluR2/3 immunoreactive cells (magenta). Right, merge image. Scale bar, 50 μm. GCL, granule cell layer; H, hilus; ML, molecular layer.

(C) Schematic of the fiber photometry setup and the EPM.

(D) Heatmap illustrating the relative time spent in different locations of a mouse. Dashed line, open arm (O); solid line, closed arm (C).

(E) Representative Ca^{2+} transient during EPM exploration.

(F) Heatmap of normalized Ca^{2+} signals corresponding to the location of a mouse.

(G) Trajectory direction and representative normalized Ca^{2+} signals corresponding to traveling routes of a mouse. O, open arm; C, closed arm.

(H) Probability distribution of averaged *Z* score of Ca^{2+} signals in open and closed arms.

(I) Comparison between the averaged Ca^{2+} signals in different arms. Lines connect data collected from the same mouse. Open arm, 2.3% ± 0.8%; closed arm, −0.6% ± 0.2%; n = 9; **p < 0.01; *Z* = −2.66; Wilcoxon signed-rank test.

(J) Experimental schematic.

(legend continued on next page)

excitation preferentially drives local INs, thereby modulating the overall GC activity (Hsu et al., 2016; Scharfman, 1995).

Accumulating evidence suggests that MCs play a potential role in stress and mood regulation. First, MCs express glucocorticoid receptors (Patel and Bulloch, 2003), which are related to anxiety- and depression-like behaviors. Novelty and stress are frequently accompanied by anxiety (Bannerman et al., 2003; Fanselow and Dong, 2010). Recent studies have demonstrated that the activity of ventral MCs increases when animals encounter a novel object (Bernstein et al., 2019) or explore a novel environment (Fredes et al., 2021), whereas it decreases if animals experience an acute, stressful condition (Moretto et al., 2017). Second, 5-HT_{2A} serotonin receptors, which play an important role in mood regulation, are expressed in MCs (Tanaka et al., 2012). Chronic administration of selective serotonin reuptake inhibitors (SSRIs) has been shown to enhance MC activity and reduce the latency to feed in the novelty-suppressed feeding test (Oh et al., 2020). Conversely, acute inhibition of MCs impairs their behavioral responses to SSRI-mediated reduction of depression-like behavior (Oh et al., 2020). However, a recent study reported a different finding. They show that inhibiting MC activity in female mice reduces the latency to feed in the novelty-suppressed feeding test (Botterill et al., 2021). Lastly and most important, selective MC degeneration in mice not only causes transient GC hyperexcitability but it also results in increased anxiety-like behavior (Jinde et al., 2012). Despite previous observations, a direct correlation between MC activity and innate anxiety-related behavior has not yet been established.

In this study, we tested the role of MCs in controlling neuronal excitability along trisynaptic circuits and their corresponding effects on anxiety states. We showed that ventral MC activity greatly increased when mice explored anxiogenic environments. Next, we determined how elevating MC activity regulated DG networks and downstream CA1 using *in vivo* juxtacellular recording. Finally, we demonstrated that chemogenetically elevating MC activity reduced avoidance behaviors in healthy mice and in mice experiencing chronic pain. Our findings support the view that MCs control anxiety-related information routing by enhancing inhibition in the DG, thereby suppressing the CA1 output and disrupting avoidance behaviors.

RESULTS

MC activity increased during open-arm exploration

To correlate MC activity with avoidance behavior in freely behaving mice, we used fiber photometry to assess the changes of Ca^{2+} levels in MCs while mice were subjected to anxiogenic environments. To express the Ca^{2+} indicator GCaMP6s in MCs selectively, adeno-associated virus (AAV) serotype 1 or 5, carrying Cre-dependent GCaMP6s, was injected into the ventral DG of *Crlr-Cre* mice, an MC-specific Cre-driver line (Jinde et al., 2012) (Figure 1A). As previously described (Jinde et al., 2012), GCaMP6s-expressing cells in the DG were restricted to the hilus (Figure 1B). The vast majority of GCaMP6s-expressing cells were immunoreactive for GluR2/3, a marker of MCs (96.6% ± 1.5%, 5 slices, 2 mice; Figure 1B), suggesting a cell-type-specific labeling of MCs. After the implantation of an optical fiber, mice were introduced into the elevated plus maze (EPM; Figure 1C), which contains well-defined boundaries for anxiogenic and non-anxiogenic environments (Calhoon and Tye, 2015; Gehrlach et al., 2019; Lee et al., 2019). Consistent with previous studies (Calhoon and Tye, 2015; Pellow et al., 1985), mice spent less time in the open arms (15% ± 4% of the total time) than in the closed arms (71% ± 5% of the total time, n = 9; p = 0.004, Wilcoxon signed-rank test, Figure 1D). Intriguingly, although Ca^{2+} signals (ΔF/F%) fluctuated during the EPM test (Figure 1E), high Ca^{2+} signals were mostly detected when the mice stayed in the open arms than when they stayed in the closed arms (Figure 1F). The Ca^{2+} signal along unidirectional routes on the EPM decreased from the open arms to the closed arms. In contrast, Ca^{2+} signals increased when the mice traveled from the closed arms to the open arms (Figure 1G). Consistent with these observations, the probability distribution of Ca^{2+} signals in the open arms was right-shifted compared to that in the closed arms at the population level (Figure 1H). Overall, the average Ca^{2+} signals in the open arms were significantly higher than those in the closed arms (Figure 1I). To understand how MC activity during exploration of open spaces relates to avoidance behavior, we quantified the average Ca^{2+} signal versus the open-arm exploration time and found a negative correlation between MC activity and open-arm exploration time (Figure S1A). Finally, it is worth noting that dorsal MCs were shown to correlate with running speed (Danielson et al., 2017). Thus, we tested the correlation between ventral MC activity and running speed. In contrast to dorsal MCs, ventral MC activity did not correlate with the animal's running speed during EPM exploration (Figures S1B–S1E). To confirm the correlation between the increased MC activity and open-arm exploration, we removed the wall of a closed arm and examined the change in Ca^{2+} activity in this new open arm (Figure S2C). As expected, mice showed avoidance of all open arms (Figure S2D). The Ca^{2+} signals were increased when mice stayed in any of the three open arms (Figures S2E–S2H). Overall, the average Ca^{2+} signals were higher when mice were in the open arms than when they were in the closed arms (Figure S2I).

To eliminate potential confounding factors such as decision making or risk assessment in the center zone, we performed another subset of experiments using the elevated zero maze

(K) Heatmap illustrating the time spent in the EZM.
(L) Representative Ca^{2+} transient during EZM exploration.
(M) Heatmap of Ca^{2+} signals corresponding to the location.
(N) Representative Ca^{2+} signals corresponding to traveling routes. Zero degrees indicated the crossing point between open and closed arms.
(O) Similar to (H), probability distribution of averaged *Z* score of Ca^{2+} signals.
(P) Similar to (I), summary plot of averaged Ca^{2+} signals. Open arm, 2.0% ± 0.5%; closed arm −0.3% ± 0.1%; n = 7; *p < 0.05; $Z = -2.37$; Wilcoxon signed-rank test.
Data are represented as mean ± SEM in (I) and (P). Data are represented as mean ± SD in (H) and (O).
See also Figures S1 and S2.

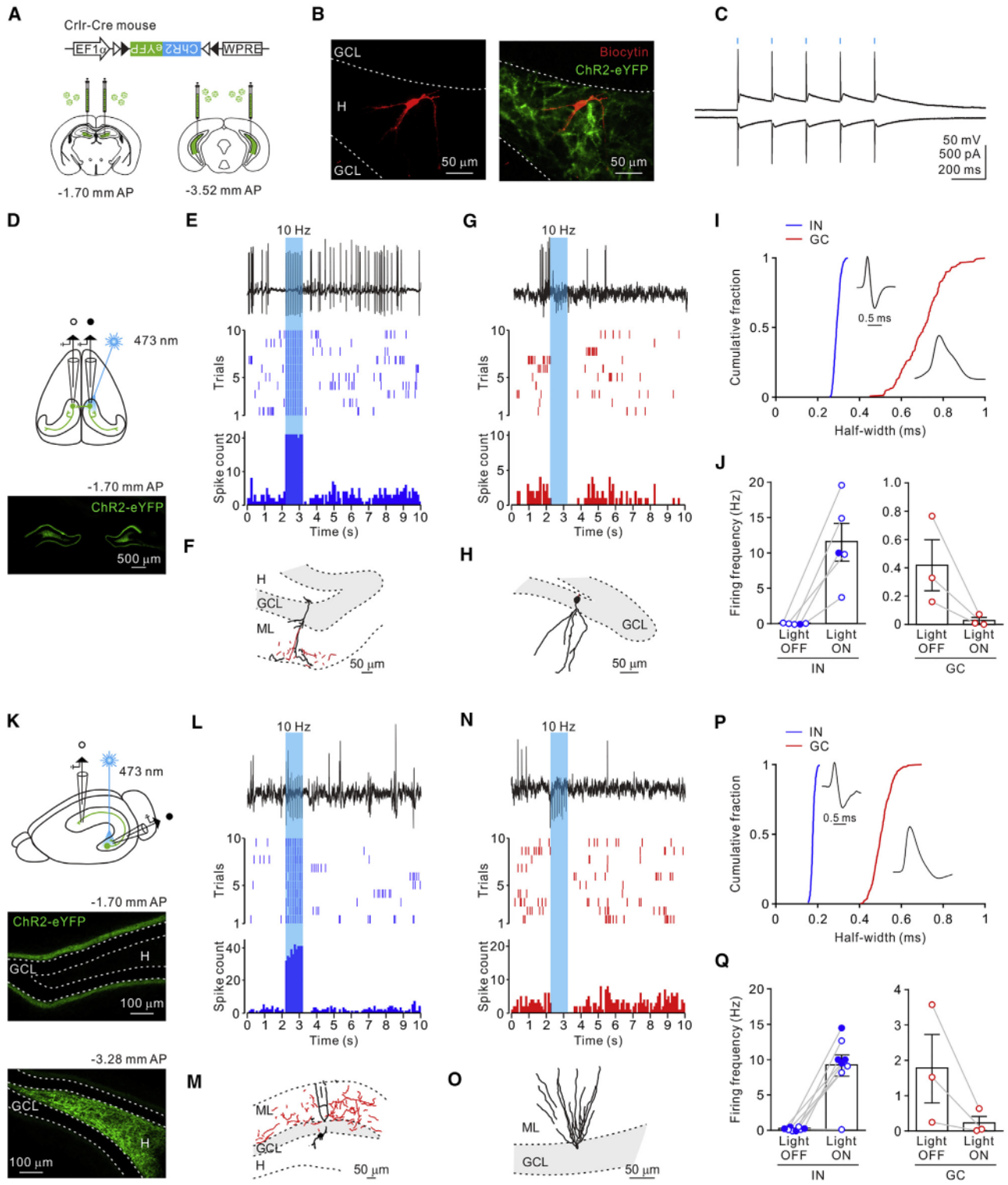

Figure 2. MC activation recruited GABAergic INs and suppressed GCs

(A) Schematic of coronal sections of the *Crlr-Cre* mouse injected with an AAV5-DIO-ChR2-eYFP into the dorsal or ventral DG bilaterally.

(B) Morphology of a biocytin-filled MC (left) and merged image of biocytin and ChR2-eYFP (right). Scale bar, 50 μm.

(C) Light-evoked spikes recorded from a ChR2-expressing MC (470 nm, 5-Hz, 5-ms light pulse) in the current-clamp mode and a ChR2-mediated photocurrent in the voltage-clamp mode.

(legend continued on next page)

(EZM; Figure 1J). Similar to the observations in the EPM, mice spent much less time in the open areas (11% ± 2% of the total time; Figure 1K), and Ca^{2+} signals were increased when mice explored the open areas (Figures 1L and 1M). Analysis of Ca^{2+} dynamics along the travel routes revealed that the Ca^{2+} signals gradually decreased when mice traveled from the open to the closed areas, whereas the Ca^{2+} signals gradually increased when mice traveled from the closed to the open areas (Figure 1N). On average, the Ca^{2+} activity of MCs was higher when mice were in the open areas than when they were in the closed areas (Figures 1O and 1P). These data indicate that MCs are more active when the animal is in an innately anxiogenic environment.

MC activation recruited GABAergic INs and suppressed GCs

Next, we investigated the circuit mechanism underlying MC activation using *in vivo* juxtacellular recording. To activate MCs at specific times, we virally expressed ChR2-eYFP in MCs in the dorsal or ventral DG (Figure 2A) and examined DG cell activity after optogenetic activation of MCs. In brain slices, brief light pulses (470 nm, 5 ms) delivered at 5 Hz evoked spikes and inward currents in ChR2-expressing MCs (Figures 2B and 2C). Next, we performed *in vivo* juxtacellular recordings of DG cells in head-fixed anesthetized mice. Putative INs exhibit a narrower spike half-width than putative GCs (Bui et al., 2018; Csicsvari et al., 1999; Diamantaki et al., 2016) (Figures 2I and 2P). Light stimulation of dorsal MCs activated putative INs in the contralateral and ipsilateral DG (Figures 2D and 2E). In contrast, putative GCs in the contralateral DG (Figure 2G) were suppressed after MC activation. After recordings, neurobiotin-filled cells were morphologically identified (Figures 2F, 2H, and S3A). Overall, all recorded INs (three morphologically identified INs of five juxtacellularly recorded cells; Figure 2J, blue circles) were activated and all of the recorded GCs (two morphologically identified GCs of three juxtacellularly recorded GCs; Figure 2J, red circles) were inhibited after dorsal MC activation.

Next, we investigated the longitudinal projections of MCs by injecting an AAV-DIO-ChR2-eYFP into the bilateral ventral DG (Figure 2K). Similar to the activation of commissural projections, 10-Hz photostimulation of ventral MCs activated most INs in the dorsal DG (one morphologically identified IN of four juxtacellularly recorded cells; Figures 2L, 2M, and 2Q, blue open circles, and S3B, left) and all INs in the ventral DG (one morphologically identified IN of four juxtacellularly recorded cells; Figure 2Q, blue filled circles). In contrast, the activation of longitudinal projections of MCs suppressed GCs (Figures 2N, 2O, and 2Q, red circles and S3B, right) in the dorsal DG. Off-target effects of photostimulation were excluded because light-evoked field responses were not detected in mice without ChR2 expression (Figures S3C–S3G). Collectively, activation of either dorsal or ventral MCs activated INs but suppressed GCs, suggesting a potential role of MCs in gating the output of the DG.

Optogenetic activation of MCs suppressed CA1 PCs

Information from the DG is finally transmitted to the CA1 through the canonical trisynaptic circuit. Next, we tested whether activating MCs can suppress hippocampal CA1 pyramidal cells (PCs) in the trisynaptic pathway after the inhibition of GCs. To achieve this, we activated ChR2-expressing MCs in the ventral DG and juxtacellularly recorded CA1 PCs (Figure 3A). The recorded neurons were electrophysiologically identified as PCs by their complex spikes (Figure 3B, box) and subsequently confirmed by post hoc morphological reconstructions (Figure 3C). Similar to GCs, the recorded CA1 PCs were suppressed in response to ventral MC stimulation in anesthetized (Figures 3Band 3D, open circles) and awake mice (Figure 3D, filled circle). Overall, the firing frequency of the PCs decreased during the light stimulation epoch (Figure 3D).

Elevating ventral MC activity decreased avoidance behaviors

Next, we asked whether elevating MC activity was sufficient to reduce avoidance behaviors. To this end, we used a

(D) Top, experimental schematic. Bottom, expression pattern of AAV5-DIO-ChR2-eYFP; scale bar, 500 μm.
(E) Top, representative trace. Middle, raster plot from representative 10 sweeps of a recorded cell. Bottom, peristimulus time histogram (PSTH) from all sweeps of a recorded cell during 10-Hz photostimulation (blue bar).
(F) Morphological reconstruction of the post hoc neurobiotin stained cell shown in (E). Somata and dendrites of a reconstructed cell were in black and the axons were in red.
(G) Similar to (E), representative data from a GC.
(H) Morphological reconstruction of the cell shown in (G).
(I) Cumulative probability distribution of spike half-width and the representative spike waveforms of the IN and GC shown in (E) and (G), respectively.
(J) Summary of the firing frequency during light-off and light-on epochs for INs (blue) and GCs (red). Open and filled circles represent the responses of dorsal DG cells to contralateral and ipsilateral MC activation, respectively. IN, light-off, 0.10 ± 0.04 Hz; light-on, 11.60 ± 2.67 Hz; n = 5; GC, light-off, 0.42 ± 0.18 Hz; light-on, 0.03 ± 0.02 Hz; n = 3.
(K) Top, experimental schematic. Center, confocal image of ChR2-eYFP expression in the inner molecular layer of the dorsal DG. Bottom, confocal image of ChR2-eYFP expression in the ventral DG. Scale bar, 100 μm.
(L) Similar to (E), representative data from an IN.
(M) Morphological reconstruction of the recorded cell in (L).
(N) Similar to (E), representative data from a GC.
(O) A morphologically reconstructed cell shown in (N).
(P) Cumulative probability distribution of spike half-width and the representative spike waveforms of the IN and GC shown in (L) and (N), respectively.
(Q) Similar to (J). Open and filled circles represent the responses of dorsal and ventral DG cells, respectively, to ventral MC activation. IN, light-off, 0.28 ± 0.08 Hz; light-on, 9.25 ± 1.50 Hz; n = 8; GC, light-off, 1.78 ± 0.97 Hz; light-on, 0.23 ± 0.20 Hz; n = 3.
Data are represented as mean ± SEM.
See also Figure S3.

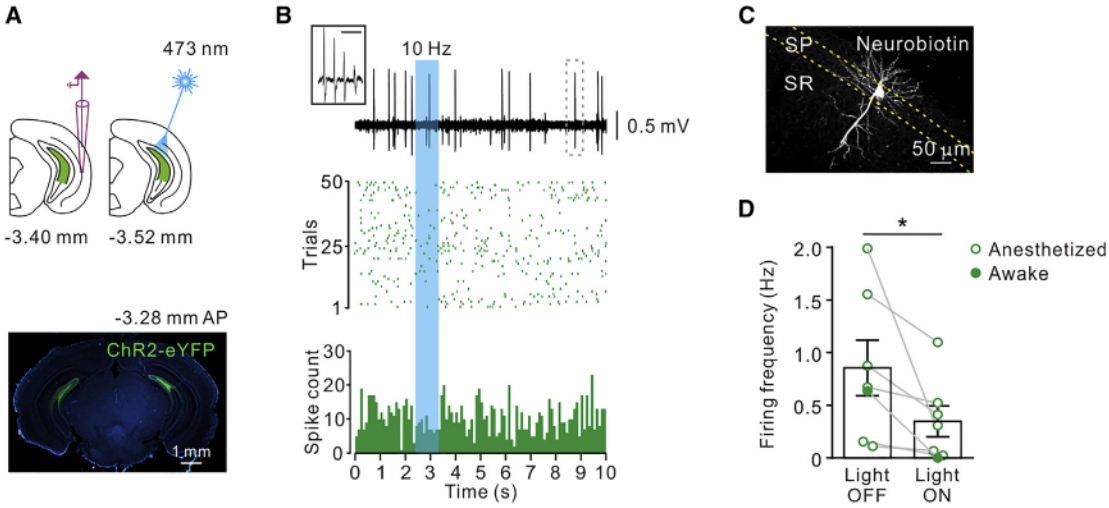

Figure 3. Optogenetic activation of MCs suppressed CA1 PCs

(A) Top, schematic of experimental configuration. Bottom, an image of ChR2-eYFP expression; scale bar, 1 mm.

(B) The responses of the CA1 PC to ventral MC stimulation. Top, representative trace of a recorded cell during the 10-Hz photostimulation (blue bar). Box, enlarged complex spikes; scale bar, 10 ms. Center, raster plot of representative spikes. Bottom, PSTH of all spikes.

(C) Confocal image of the post hoc neurobiotin-stained cell shown in (B). Scale bar, 50 μm.

(D) Summary of the averaged firing frequency during light-off and light-on epochs. Filled and open circles represent the data collected from awake and anesthetized mice, respectively. Light-off, 0.9 ± 0.3 Hz; light-on, 0.3 ± 0.1 Hz; n = 7; p = 0.016; $Z = -2.3$; Wilcoxon signed-rank test.

Data are represented as mean ± SEM.

chemogenetic approach to manipulate MC activity selectively. An AAV5 carrying Cre-dependent eDREADD (hM3Dq-mCherry) or control (mCherry) was injected into the bilateral ventral DG of *Crlr-Cre* mice (Figures 4A and 4B). Whole-cell patch-clamp recordings showed that hM3Dq-mCherry-expressing neurons in brain slices were depolarized after bath application of 5 μM clozapine N-oxide (CNO) (Figure 4C). Elevating ventral MC activity significantly increased the time that mice spent in the open arms relative to the mCherry control group in the EPM (Figure 4D). The total travel distances were similar in both groups (Figure 4D). Thus, elevating ventral MC activity reduced open-arm avoidance without altering locomotion. Similar to the EPM test, mice spent more time at the center of the open field upon ventral MC activation in the open field test (OFT; Figure 4E). Locomotion did not differ during ventral MC activation (Figure 4E). Furthermore, elevating ventral MC activity markedly decreased the number of buried marbles compared to that in the mCherry control groups (Figure 4F). In addition, no significant sex differences were observed in any of the behavioral tasks (Table S1). Thus, elevating ventral MC activity is enough to the generation of anxiolytic effects.

To examine whether the neuronal activity of MCs is essential for regulating avoidance behaviors, we chemogenetically inhibited MC activity by injecting an AAV5-carrying Cre-dependent iDREADD (hM4Di-mCherry) into *Crlr-Cre* mice. Intriguingly, decreasing ventral MC activity had no impact on avoidance behaviors (Figures S4A–S4D). Similar results were obtained when MCs were strongly inactivated using an optogenetic approach (Figures S4E–S4J), suggesting that ventral MCs are not required for normal avoidance behaviors.

Furthermore, we considered whether dorsal MC activity also participates in mediating avoidance behaviors. Notably, elevating dorsal MC activity failed to cause any changes in the open-arm time and center field time in the EPM and OFT, respectively (Figures S5A and S5B). However, mice buried fewer marbles in the marble-burying test (Figure S5C). The travel distance in the eDREADD group was similar to that of the mCherry group in the EPM and OFT tests (Figures S5A and S5B). In addition, decreasing dorsal MC activity had little effect on avoidance behaviors (Figures S5D–S5F). The less-consistent behavioral results suggest a lesser role of dorsal MCs in generating avoidance behaviors.

Elevating MC activity decreased avoidance behaviors in chronic pain

Chronic pain causes emotional changes such as anxiety and depression (Bushnell et al., 2013). We further corroborated the MC-mediated anxiolytic effect in a mouse model of fibromyalgia (FM) (DeSantana et al., 2013; Sharma et al., 2009; Sluka et al., 2001). Similar to patients with FM, FM-like mice display comorbid anxiodepressive symptoms (Liu et al., 2014b; Thieme et al., 2004). To model FM, acidic saline was administered unilaterally into the gastrocnemius muscle of mice immediately after the von Frey test for the baseline (BL) on days 0 and 3 (Figure 5A). In contrast to the FM group, mice that received normal saline injections served as the sham group. The hind paw withdrawal (PW) threshold in the FM group was significantly reduced after acidic saline injection on the day after the BL test, and the mechanical allodynia persisted up to 14 days after the second acidic saline injection in the FM group, indicating the

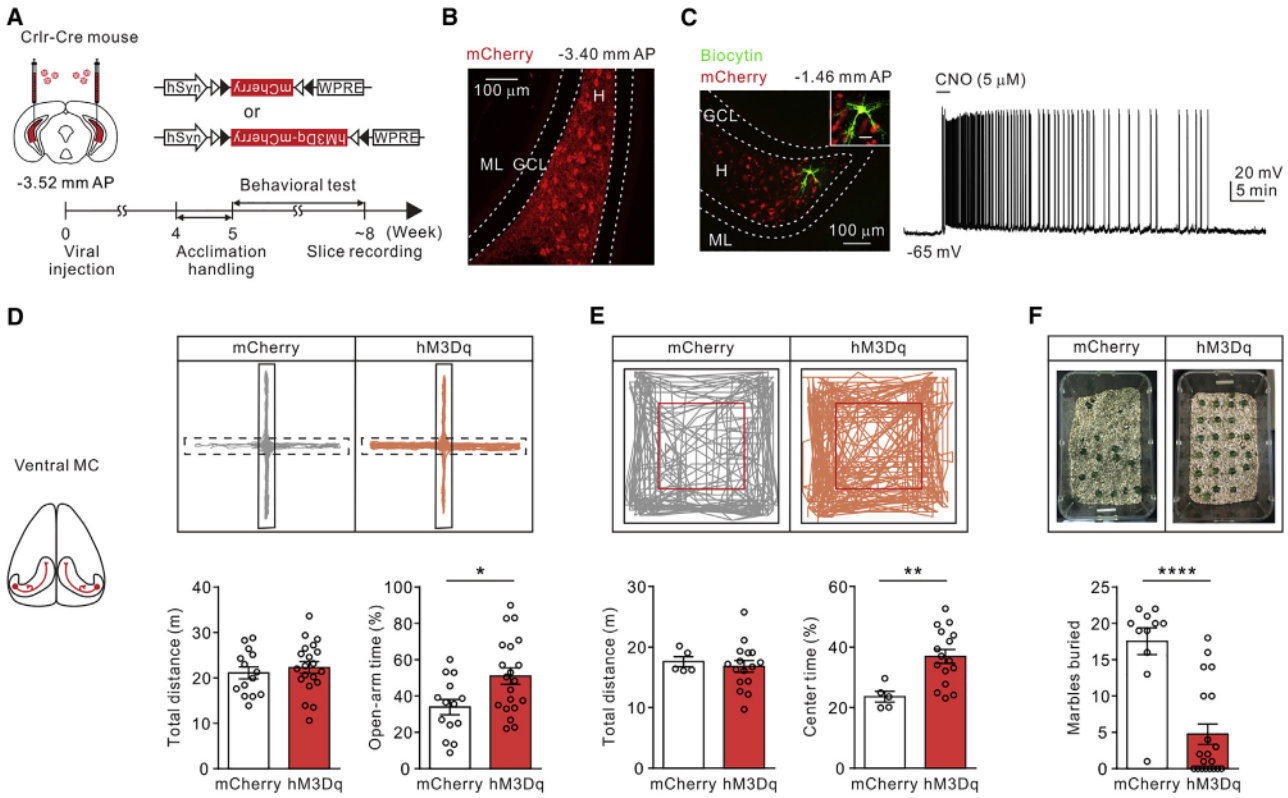

Figure 4. Elevating MC activity decreased avoidance behaviors

(A) Experimental schematic and timeline.

(B) Confocal image of hM3Dq-expressing MCs in the ventral DG. Scale bar, 100 μm.

(C) Left, confocal images of a biocytin-filled MC, which expressed mCherry; scale bar, 100 μm. Box, high magnification of the labeled MC. Scale bar, 10 μm. Right, membrane potential changes of a hM3Dq-expressing MC recorded in the presence of kynurenic acid (2 mM) and gabazine (1 μM) in response to bath-applied CNO (5 μM).

(D) Top, representative travel tracks of each group in the EPM. Bottom, summary of travel distance and open-arm time. Total distance, n = 14 for mCherry, 21.1 ± 1.3 m; n = 20 for hM3Dq, 22.3 ± 1.3 m; p = 0.45; *U* = 118. Open-arm time, n = 14 for mCherry, 33.9% ± 4.2%; n = 20 for hM3Dq, 51.0% ± 4.6%; *p < 0.05; *U* = 81; Mann-Whitney test.

(E) Top, representative travel tracks of each group in the OFT. Bottom, summary of travel distance and center time. Total distance, n = 5 for mCherry, 17.6 ± 0.8; n = 16 for hM3Dq, 16.8 ± 1.0 m; p = 0.78; *U* = 36. Center time, n = 5 for mCherry, 23.6 ± 1.8; n = 16 for hM3Dq, 36.9% ± 2.3%; **p < 0.01; *U* = 7.5; Mann-Whitney test.

(F) Top, representative results of the marble-burying test. Bottom, summary of the marble-burying test. n = 11 for mCherry, 17.6 ± 1.8; n = 20 for hM3Dq, 4.8 ± 1.4; ****p < 0.0001; *U* = 16.5; Mann-Whitney test.

Data are represented as mean ± SEM.

See also Figures S4 and S5.

development of chronic pain (Figure 5A). Compared to the sham group, FM mice spent less time in the open arm of the EPM (Figure 5B) and buried more marbles in the marble-burying test (Figure 5C), suggesting increased avoidance behavior. It is worth noting that the total travel distances were similar between the FM and sham groups in the EPM test (Figure 5B).

To determine whether elevating MC activity was sufficient to alleviate avoidance behaviors in FM mice, we induced chronic pain in both mCherry- and hM3Dq-expressing *Crlr-Cre* mice (Figure 5D). Notably, the PW threshold did not change after elevating MC activity in FM-mCherry and FM-hM3Dq mice (day 16; Figure 5E). Next, we tested the anxiolytic effect of MC activation on FM mice. Chemogenetic activation of MCs significantly increased the open-arm time of FM-hM3Dq mice in the EPM (Figure 5F). The total travel distances between these two groups were not different (Figure 5F). Similarly, FM-hM3Dq mice significantly buried a fewer number of marbles (Figure 5G). Collectively, enhancing ventral MC activity reduced avoidance behaviors in FM mice without altering mechanical hypersensitivity.

Gating model for MC-mediated anxiolytic effects

Finally, we propose a circuit-based model to explain how MCs decrease the HPC output via inhibiting DG GCs and CA1 PCs and thereby reduce avoidance behaviors. In this model (Figure 6A), anxiety-related information is transferred from the cortex to the DG, where GCs fire action potentials to encode valence-related contextual information during exploration of

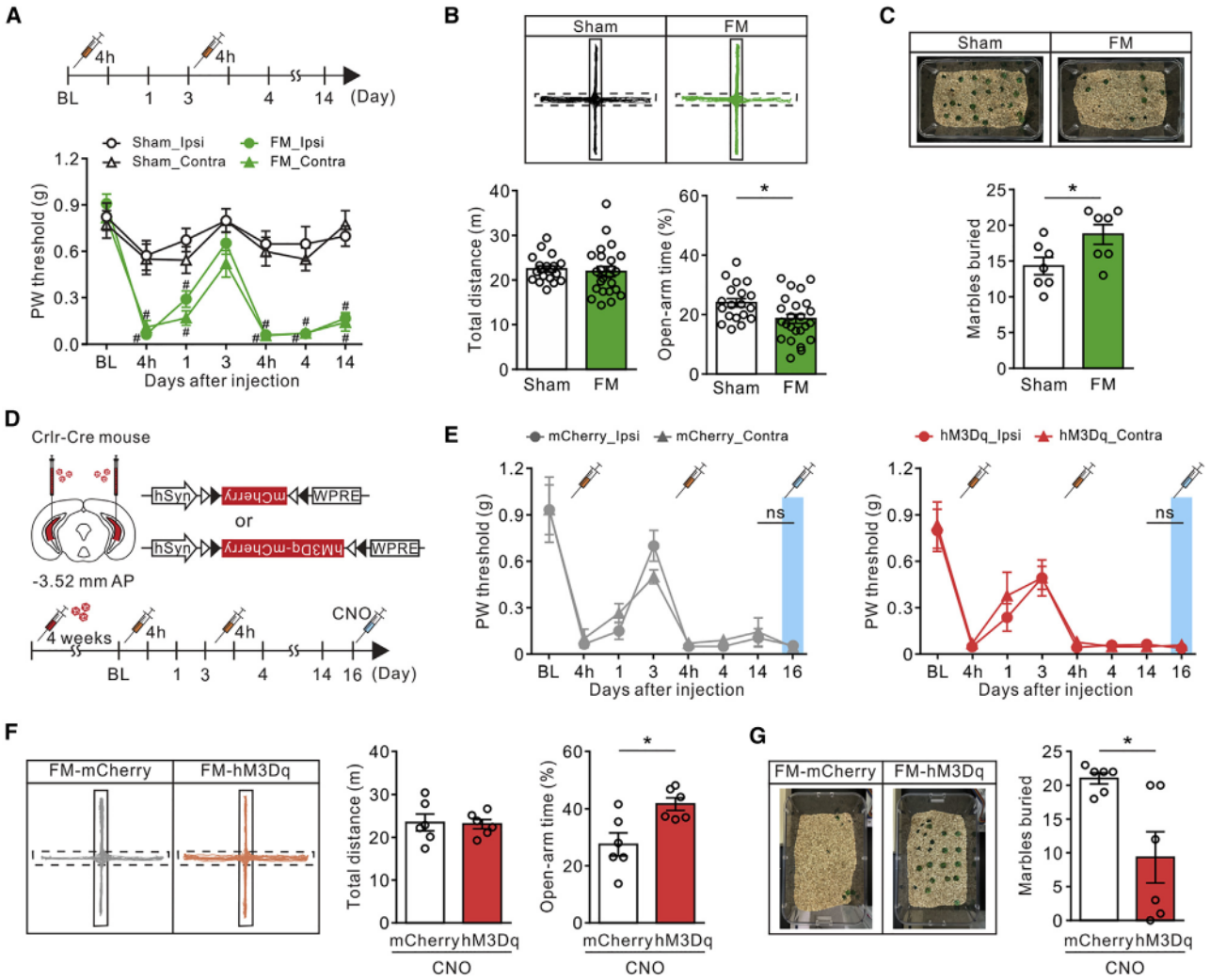

Figure 5. Enhancing MC activity alleviated heightened avoidance behavior in chronic pain

(A) Top, FM induction protocol. Bottom, PW thresholds at different time points. Group effect of ipsilateral hind paws, $F(1,17) = 84.95$; $p < 0.0001$; group effect of contralateral hind paws, $F(1,17) = 40.18$; $p < 0.0001$. $^{\#}p < 0.0001$, compared to BL; $\alpha = 0.05$; 2-way ANOVA with Bonferroni post hoc test.

(B) Top, representative travel tracks of sham and FM in the EPM. Bottom, total travel distance and open-arm time of sham and FM groups. Total distance, n = 19 for sham, 22.5 ± 1.4 m; n = 24 for FM, 18.6 ± 1.5 m; p = 0.36; U = 190; open-arm time, n = 19 for sham, 23.9% ± 1.4%; n = 24 for FM, 18.6% ± 1.5%; $^{*}p < 0.05$; $U = 131$; Mann-Whitney test.

(C) Top, representative results of the marble-burying test. Bottom, summary of the marble-burying test. n = 7 for sham, 14.3 ± 1.2; n = 7 for FM, 18.7 ± 1.4; $^{*}p < 0.05$; $U = 9$; Mann-Whitney test.

(D) Experimental schematic and timeline.

(E) PW threshold of mCherry FM mice (left, n = 6; time effect, $F(7,70) = 36.16$; $p < 0.0001$; ipsi_day14, 0.11 ± 0.06 g; ipsi_day16, 0.06 ± 0.01 g; $p > 0.99$; contra_day14, 0.14 ± 0.09 g; contra_day16, 0.05 ± 0.01 g; $p > 0.99$) and hM3Dq FM mice (right, n = 6; time effect, $F(7,70) = 33.56$; $p < 0.0001$; ipsi_day14, 0.07 ± 0.02 g; ipsi_day16, 0.04 ± 0.00 g; $p > 0.99$; contra_day14, 0.05 ± 0.01 g; contra_day16, 0.06 ± 0.02 g; $p > 0.99$); ns, no significant difference; $\alpha = 0.05$; 2-way ANOVA with Bonferroni post hoc test.

(F) Left, representative tracks of EPM. Right, summary of total distance and open-arm time. Total distance, n = 6 for mCherry-FM, 23.4 ± 2.0 m; n = 6 for hM3Dq-FM, 23.1 ± 1.1 m; $p > 0.999$; $U = 18$; open-arm time, n = 6 for mCherry-FM, 27.4% ± 4.0%; n = 6 for hM3Dq-FM, 41.6% ± 2.2%; $^{*}p < 0.05$, $U = 3$, Mann-Whitney test.

(G) Left, representative data of the marble-burying test. Right, summary of the marble-burying test. n = 6 for mCherry-FM, 21.0 ± 0.8; n = 6 for hM3Dq-FM, 8.9 ± 3.2; $^{*}p < 0.05$; $U = 4$; Mann-Whitney test.

Data are represented as mean ± SEM.

the open spaces. In the DG, GCs make strong monosynaptic excitatory connections with MCs via their mossy fibers. Therefore, GC firing not only sends the anxiogenic signal to the downstream CA3 and CA1 areas but it also activates MCs. This model is in line with a previous report by Jimenez et al. (2018) that ventral CA1 neurons preferentially fire in open areas and are hence called anxiety cells. Experimentally activating MCs using optogenetics or chemogenetics (Figure 6B)

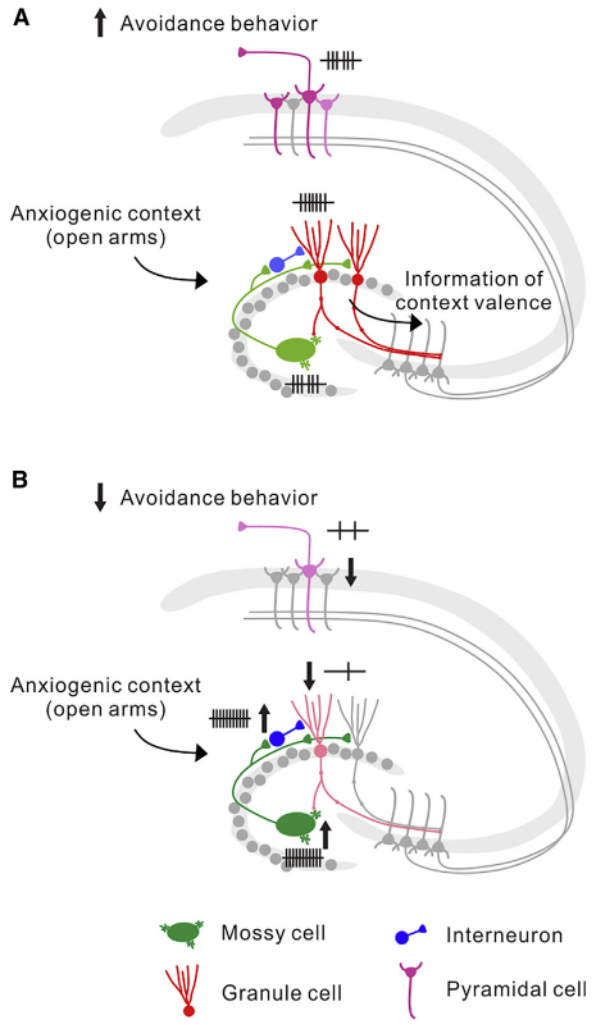

Figure 6. MC gates in anxiety-related information routing along hippocampal circuits

(A) While mice explore the EPM or EZM under normal conditions, information of anxiogenic contexts finally leads to increased CA1 output and enhanced avoidance behavior.

(B) Activating MCs in manipulated mice can suppress the DG-CA3-CA1 pathway through enhancement of local inhibitory INs and finally generates anxiolytic effects.

suppresses GCs via local INs and prevents the flow of information from GCs to the downstream CA3 PCs and CA1 PCs. The decreased activity of ventral CA1 PCs (or anxiety cells) fails to encode anxiety-related information and leads to reduced avoidance behaviors (Jimenez et al., 2018; Padilla-Coreano et al., 2016).

DISCUSSION

In this study, we observed anxiety-related increases in MC activity and demonstrated that experimentally enhancing MC activity using the chemogenetic approach reduced avoidance behaviors. This apparent discrepancy requires an explanation. Our findings suggest a model (Figure 6) in which behaviorally relevant contextual information from the entorhinal cortex is transferred to the DG, where GCs and their major local target cells, the MCs, fire action potentials to encode information with a negative valence. Therefore, higher MC activity signals a higher anxiogenic valence. MC activity was negatively correlated with open arm exploration time (Figure S1A). The information of anxiogenic contexts is then eventually sent to the CA1 output neurons and their targets, which mediate avoidance behavior.

The changes in MC activity observed with fiber photometry were highly acute and contextually specific. However, DREADD-mediated membrane depolarization is sustained and independent of the context (Sternson and Roth, 2014). Therefore, the effect of chemogenetic manipulation cannot mimic acute changes in MC activity. In light of these differences, we acknowledge a potential caveat in the interpretation of the results of the chemogenetic experiment. As suggested by our model, the effect of chemogenetic activation of MCs on avoidance behavior involves the sustained suppression of anxiety-related information routing from the DG to the CA3 (Figure 6B). Under normal conditions, information about anxiogenic contexts is encoded by neuronal activity patterns (Figure 6A). In the DG circuitry, GC excitation activates local INs and MCs, which further modulate GC activity. Therefore, both MCs and INs shape GC spiking patterns (Hsu et al., 2016; Lee et al., 2016) and contribute to the representation of behaviorally related information. To mimic acute changes in MC activity observed with fiber photometry, activating MCs at frequencies close to physiological MC activity in the anxiogenic contexts using an optogenetic approach when mice stay in closed arms may be more appropriate.

Our previous study (Hsu et al., 2016) demonstrated that MCs project contralaterally and inhibit GCs by exciting local GABAergic INs. Several lines of evidence suggest that GABA-mediated inhibition by MC activation is implicated in anxiety suppression. First, selective MC degeneration causes GC hyperexcitability and increases anxiety (Jinde et al., 2012). Second, physical exercise-induced suppression of anxiety is associated with a reduction in stress-induced GC activation and enhanced inhibition in the DG (Schoenfeld et al., 2013). Third, chemogenetic activation of parvalbumin-positive INs in the DG induces an anxiolytic effect (Zou et al., 2016). Lastly, selective deletion of α2-containing $GABA_A$ receptors in DG GCs and CA3 principal neurons results in heightened anxiety (Engin et al., 2016). The information processed in the DG is relayed to the CA1 region through the canonical trisynaptic DG-CA3-CA1 circuit. Therefore, the DG represents the starting point, whereas the CA1 represents the ending point of the intrahippocampal circuit and the primary source of extrinsic hippocampal-cortical projections. To our knowledge, our *in vivo* juxtacellular recording is the first to demonstrate that MC activation via regulating DG excitability can influence the HPC output, which is tightly linked to anxiety-related behavior (Padilla-Coreano et al., 2016; Jimenez et al., 2018).

Multiple circuit mechanisms have been shown to determine the state of anxiety (Kim et al., 2013; Parfitt et al., 2017). A subpopulation of lateral hypothalamus (LH)-projecting PCs in the CA1 region of the vHPC (vCA1), also called anxiety cells, was shown to respond to anxiogenic stimuli and to control anxiety-related

behavior. Selective enhancement or suppression of the activity of these neurons bidirectionally regulates the anxiety state (Jimenez et al., 2018). Additional circuits linking the vHPC to non-limbic structures that are also involved in anxiety regulation have been described previously (Adhikari et al., 2010; Bazelot et al., 2015; Ciocchi et al., 2015; Padilla-Coreano et al., 2016). Similar to LH-projecting vCA1 cells, the inhibition of medial prefrontal cortex (mPFC)-projecting vCA1 cells decreases avoidance behavior (Padilla-Coreano et al., 2016). Consequently, selective information routing along the vHPC circuits and the final balance between anxiogenic- and anxiolytic-like actions is critical in modulating the expression of emotional behaviors. Consistent with this notion, our findings showed that activating MCs through the enhancement of inhibitory mechanisms within the DG can suppress the DG-CA3-CA1 pathway, thereby contributing to an anxiolytic effect (Figure 6B). Notably, most vCA1 neurons project to only one downstream target and emerge in a non-overlapping pattern (Gergues et al., 2020; Jimenez et al., 2018; Jin and Maren, 2015; Kim and Cho, 2017; Parfitt et al., 2017). In addition, distinct target-projecting vCA1 neuronal populations are topographically distributed (Gergues et al., 2020). The exact population of vCA1 PCs that is inhibited by MC activation remains to be explored.

In addition to multiple inputs from the GCs (Amaral, 1978; Williams et al., 2007), MCs receive information from several upstream areas, including the medial septum-diagonal band complex, the lateral entorhinal cortex, and the CA3 region (Azevedo et al., 2019; Sun et al., 2017). To reveal the circuit mechanism underlying MC activation in anxiogenic environments, further investigation of local and long-range circuit connections to ventral MCs is needed. For example, the medial septum, which is involved in anxiety, contains a population of MC-projecting cholinergic neurons (Deller et al., 1999; Lübke et al., 1997; Sun et al., 2017).

Within the hippocampal formation, the vHPC has been linked to affective and motivated behaviors because of its connections with several limbic structures (Bannerman et al., 2003; Barkus et al., 2010; Ciocchi et al., 2015; Fanselow and Dong, 2010; Weeden et al., 2015), whereas the dorsal HPC (dHPC) is associated with spatial learning and navigation due to its projections to the subiculum and other cortical areas (Fanselow and Dong, 2010; Moser et al., 1995; O'Keefe and Dostrovsky, 1971). MCs in the dHPC are anatomically, immunochemically, transcriptomically, and physiologically different from MCs in the vHPC (Cembrowski et al., 2016; Fujise et al., 1998; Fujise and Kosaka, 1999; Houser et al., 2021; Jinno et al., 2003). First, there are fewer MCs in the dHPC (Fujise and Kosaka, 1999). Second, dorsal MCs exhibit larger and more complex thorny excrescences than ventral MCs (Houser et al., 2021). Third, only ventral MCs selectively express calretinin (Fujise et al., 1998). Fourth, dorsal MCs exhibit a higher spontaneous excitatory postsynaptic potential (EPSP) frequency and a larger EPSP amplitude (Jinno et al., 2003). Lastly, ventral MCs show higher spontaneous spike activity than dorsal MCs (Jinno et al., 2003). Our study further demonstrates that ventral MCs, rather than dorsal MCs, play an active role in regulating avoidance behavior.

Hippocampal oscillations can modulate anxiety (Çalışkan and Stork, 2018). Increasing the theta and gamma oscillations or the theta/gamma coupling may generate anxiety-like behaviors (Albrecht et al., 2013; Dunkley et al., 2015; Khemka et al., 2017). Moreover, synchrony between CA1 neurons and the mPFC increases during anxiety (Adhikari et al., 2010). Consistently, our *in vivo* juxta-recording showed the suppression of CA1 PC activity after MC activation (Figure 3). Although accumulating evidence supports that increased DG and CA1 excitability is associated with negative emotions, a recent study by Kheirbek et al. (2013) showed that optogenetic activation of GCs of the ventral DG decreases anxiety-like behavior. This effect is unlikely to occur under physiological conditions because in their study ~30%–50% of GCs were cFos$^+$ cells after optogenetic stimulation of GCs in POMC-ChR2 mice. Interestingly, a recent study by the same group (Anacker et al., 2018) showed the opposite result with chemogenetic manipulation, in which inhibition of mature GCs decreased stress-induced anxiety-like behavior.

The ability to recognize dangerous situations and environments is crucial for survival, but overestimating risk can lead to pathological avoidance of normal activities and can lead to anxiety disorders (Gagne et al., 2018; Jovanovic and Ressler, 2010). Increased adult neurogenesis inhibits the population of mature developmentally born GCs and supports pattern separation, reduces memory interference, and enables reversal learning in both neutral and fearful situations (Anacker and Hen, 2017; Anacker et al., 2018). Hilar MCs serve as the only glutamatergic input to young adult-born GCs during adult neurogenesis (Chancey et al., 2014). In addition to direct recruitment of inhibitory INs by MCs, it is likely that MC activation suppresses anxiety through young adult-born GC-mediated inhibition. Whether they are mediated by different populations of inhibitory INs remains unclear. Further studies are also needed to investigate whether prolonged MC stimulation can further reduce anxiety through enhanced hippocampal neurogenesis.

STAR★METHODS

Detailed methods are provided in the online version of this paper and include the following:

- KEY RESOURCES TABLE
- RESOURCE AVAILABILITY
  - Lead contact
  - Materials availability
  - Data and code availability
- EXPERIMENTAL MODEL AND SUBJECT DETAILS
  - Animal model
  - Fibromyalgia model
- METHOD DETAILS
  - Viruses
  - Stereotaxic injection
  - Fiber optic implantation
  - *In vivo* fiber photometry
  - Behavioral tests
  - *In vivo* juxtacellular recording
  - Slice preparation and patch-clamp recording
  - Solutions and drugs
  - Immunohistochemistry and histology
- QUANTIFICATION AND STATISTICAL ANALYSIS

SUPPLEMENTAL INFORMATION

Supplemental information can be found online at https://doi.org/10.1016/j.celrep.2021.109702.

ACKNOWLEDGMENTS

We thank F. Ferraguti (University of Innsbruck, Austria), A. Dominique (University of Liege, Belgium), H.J. Cheng (Academia Sinica, Taiwan), H. Lu (George Washington University, USA), C.H. Wang (RIKEN, Japan), and J. Song (University of North Carolina, USA) for commenting on an earlier version of the manuscript, and all of the members of the Lien lab for insightful discussions. This work was financially supported by the Brain Research Center, National Yang Ming Chiao Tung University from the Featured Areas Research Center Program within the framework of the Higher Education Sprout Project by the Ministry of Education in Taiwan, National Health Research Institutes (NHRI-EX110-10814NI), and the Ministry of Science and Technology (MOST; 106-2320-B-010-011-MY3, 106-2923-B-010-001-MY3, 108-2923-B-010-001-MY2, 108-2911-I-010-504, 108-2321-B-010-009-MY2, 108-2320-B-010-026-MY3, 108-2638-B-010-002-MY2, 110-2321-B-010-006, MOST-HAS Project-based Personnel Exchange Program 105-2911-I-010-508) in Taiwan.

AUTHOR CONTRIBUTIONS

Conceptualization, K.-Y.W., J.-K.C., and C.-C.L.; methodology, K.-Y.W., R.G.A., G.T., and C.-C.L.; investigation, K.-Y.W. and W.-Y.W.; formal analysis, K.-Y.W., J.-W.W., W.-Y.W., and C.-C.C.; writing – original draft, K.-Y.W., J.-K.C., and C.-C.L.; writing – review & editing, K.-Y.W., J.-W.W., C.-C.C., and C.-C.L.; resources, K.N.; funding acquisition, C.-C.L.; supervision, C.-C.L.

DECLARATION OF INTERESTS

The authors declare no competing interests.

Received: May 7, 2021
Revised: July 9, 2021
Accepted: August 20, 2021
Published: September 14, 2021

REFERENCES

Adhikari, A., Topiwala, M.A., and Gordon, J.A. (2010). Synchronized activity between the ventral hippocampus and the medial prefrontal cortex during anxiety. Neuron *65*, 257–269.

Albrecht, A., Çalışkan, G., Oitzl, M.S., Heinemann, U., and Stork, O. (2013). Long-lasting increase of corticosterone after fear memory reactivation: anxiolytic effects and network activity modulation in the ventral hippocampus. Neuropsychopharmacology *38*, 386–394.

Amaral, D.G. (1978). A Golgi study of cell types in the hilar region of the hippocampus in the rat. J. Comp. Neurol. *182*, 851–914.

Amaral, D.G., Scharfman, H.E., and Lavenex, P. (2007). The dentate gyrus: fundamental neuroanatomical organization (dentate gyrus for dummies). Prog. Brain Res. *163*, 3–22.

Anacker, C., and Hen, R. (2017). Adult hippocampal neurogenesis and cognitive flexibility - linking memory and mood. Nat. Rev. Neurosci. *18*, 335–346.

Anacker, C., Luna, V.M., Stevens, G.S., Millette, A., Shores, R., Jimenez, J.C., Chen, B., and Hen, R. (2018). Hippocampal neurogenesis confers stress resilience by inhibiting the ventral dentate gyrus. Nature *559*, 98–102.

Azevedo, E.P., Pomeranz, L., Cheng, J., Schneeberger, M., Vaughan, R., Stern, S.A., Tan, B., Doerig, K., Greengard, P., and Friedman, J.M. (2019). A role of Drd2 hippocampal neurons in context-dependent food intake. Neuron *102*, 873–886.e5.

Bannerman, D.M., Grubb, M., Deacon, R.M., Yee, B.K., Feldon, J., and Rawlins, J.N. (2003). Ventral hippocampal lesions affect anxiety but not spatial learning. Behav. Brain Res. *139*, 197–213.

Barkus, C., McHugh, S.B., Sprengel, R., Seeburg, P.H., Rawlins, J.N., and Bannerman, D.M. (2010). Hippocampal NMDA receptors and anxiety: at the interface between cognition and emotion. Eur. J. Pharmacol. *626*, 49–56.

Bazelot, M., Bocchio, M., Kasugai, Y., Fischer, D., Dodson, P.D., Ferraguti, F., and Capogna, M. (2015). Hippocampal theta input to the amygdala shapes feedforward inhibition to gate heterosynaptic plasticity. Neuron *87*, 1290–1303.

Bernstein, H.L., Lu, Y.L., Botterill, J.J., and Scharfman, H.E. (2019). Novelty and novel objects increase c-Fos immunoreactivity in mossy cells in the mouse dentate gyrus. Neural Plast. *2019*, 1815371.

Blackburn-Munro, G., and Jensen, B.S. (2003). The anticonvulsant retigabine attenuates nociceptive behaviours in rat models of persistent and neuropathic pain. Eur. J. Pharmacol. *460*, 109–116.

Botterill, J.J., Vinod, K.Y., Gerencer, K.J., Teixeira, C.M., LaFrancois, J.J., and Scharfman, H.E. (2021). Bidirectional regulation of cognitive and anxiety-like behaviors by dentate gyrus mossy cells in male and female mice. J. Neurosci. *41*, 2475–2495.

Bui, A.D., Nguyen, T.M., Limouse, C., Kim, H.K., Szabo, G.G., Felong, S., Maroso, M., and Soltesz, I. (2018). Dentate gyrus mossy cells control spontaneous convulsive seizures and spatial memory. Science *359*, 787–790.

Burghardt, N.S., Park, E.H., Hen, R., and Fenton, A.A. (2012). Adult-born hippocampal neurons promote cognitive flexibility in mice. Hippocampus *22*, 1795–1808.

Bushnell, M.C., Ceko, M., and Low, L.A. (2013). Cognitive and emotional control of pain and its disruption in chronic pain. Nat. Rev. Neurosci. *14*, 502–511.

Calhoon, G.G., and Tye, K.M. (2015). Resolving the neural circuits of anxiety. Nat. Neurosci. *18*, 1394–1404.

Çalışkan, G., and Stork, O. (2018). Hippocampal network oscillations as mediators of behavioural metaplasticity: insights from emotional learning. Neurobiol. Learn. Mem. *154*, 37–53.

Cembrowski, M.S., Wang, L., Sugino, K., Shields, B.C., and Spruston, N. (2016). Hipposeq: a comprehensive RNA-seq database of gene expression in hippocampal principal neurons. eLife *5*, e14997.

Chancey, J.H., Poulsen, D.J., Wadiche, J.I., and Overstreet-Wadiche, L. (2014). Hilar mossy cells provide the first glutamatergic synapses to adult-born dentate granule cells. J. Neurosci. *34*, 2349–2354.

Chen, T.W., Wardill, T.J., Sun, Y., Pulver, S.R., Renninger, S.L., Baohan, A., Schreiter, E.R., Kerr, R.A., Orger, M.B., Jayaraman, V., et al. (2013). Ultrasensitive fluorescent proteins for imaging neuronal activity. Nature *499*, 295–300.

Christian, K.M., Song, H., and Ming, G.L. (2014). Functions and dysfunctions of adult hippocampal neurogenesis. Annu. Rev. Neurosci. *37*, 243–262.

Ciocchi, S., Passecker, J., Malagon-Vina, H., Mikus, N., and Klausberger, T. (2015). Brain computation. Selective information routing by ventral hippocampal CA1 projection neurons. Science *348*, 560–563.

Csicsvari, J., Hirase, H., Czurkó, A., Mamiya, A., and Buzsáki, G. (1999). Oscillatory coupling of hippocampal pyramidal cells and interneurons in the behaving Rat. J. Neurosci. *19*, 274–287.

Danielson, N.B., Turi, G.F., Ladow, M., Chavlis, S., Petrantonakis, P.C., Poirazi, P., and Losonczy, A. (2017). In vivo imaging of dentate gyrus mossy cells in behaving mice. Neuron *93*, 552–559.e4.

Deller, T., Katona, I., Cozzari, C., Frotscher, M., and Freund, T.F. (1999). Cholinergic innervation of mossy cells in the rat fascia dentata. Hippocampus *9*, 314–320.

Deng, W., Aimone, J.B., and Gage, F.H. (2010). New neurons and new memories: how does adult hippocampal neurogenesis affect learning and memory? Nat. Rev. Neurosci. *11*, 339–350.

DeSantana, J.M., da Cruz, K.M., and Sluka, K.A. (2013). Animal models of fibromyalgia. Arthritis Res. Ther. *15*, 222.

Diamantaki, M., Frey, M., Berens, P., Preston-Ferrer, P., and Burgalossi, A. (2016). Sparse activity of identified dentate granule cells during spatial exploration. eLife *5*, e20252.

Dong, Z., Chen, W., Chen, C., Wang, H., Cui, W., Tan, Z., Robinson, H., Gao, N., Luo, B., Zhang, L., et al. (2020). CUL3 deficiency causes social deficits and anxiety-like behaviors by impairing excitation-inhibition balance through the promotion of Cap-dependent translation. Neuron *105*, 475–490.e6.

Dunkley, B.T., Doesburg, S.M., Jetly, R., Sedge, P.A., Pang, E.W., and Taylor, M.J. (2015). Characterising intra- and inter-intrinsic network synchrony in combat-related post-traumatic stress disorder. Psychiatry Res. *234*, 172–181.

Engin, E., Smith, K.S., Gao, Y., Nagy, D., Foster, R.A., Tsvetkov, E., Keist, R., Crestani, F., Fritschy, J.M., Bolshakov, V.Y., et al. (2016). Modulation of anxiety and fear via distinct intrahippocampal circuits. eLife *5*, e14120.

Fanselow, M.S., and Dong, H.W. (2010). Are the dorsal and ventral hippocampus functionally distinct structures? Neuron *65*, 7–19.

Fredes, F., Silva, M.A., Koppensteiner, P., Kobayashi, K., Joesch, M., and Shigemoto, R. (2021). Ventro-dorsal hippocampal pathway gates novelty-induced contextual memory formation. Curr. Biol. *31*, 25–38.e5.

Fujise, N., and Kosaka, T. (1999). Mossy cells in the mouse dentate gyrus: identification in the dorsal hilus and their distribution along the dorsoventral axis. Brain Res. *816*, 500–511.

Fujise, N., Liu, Y., Hori, N., and Kosaka, T. (1998). Distribution of calretinin immunoreactivity in the mouse dentate gyrus: II. Mossy cells, with special reference to their dorsoventral difference in calretinin immunoreactivity. Neuroscience *82*, 181–200.

Gagne, C., Dayan, P., and Bishop, S.J. (2018). When planning to survive goes wrong: predicting the future and replaying the past in anxiety and PTSD. Curr. Opin. Behav. Sci. *24*, 89–95.

Gehrlach, D.A., Dolensek, N., Klein, A.S., Roy Chowdhury, R., Matthys, A., Junghänel, M., Gaitanos, T.N., Podgornik, A., Black, T.D., Reddy Vaka, N., et al. (2019). Aversive state processing in the posterior insular cortex. Nat. Neurosci. *22*, 1424–1437.

Gergues, M.M., Han, K.J., Choi, H.S., Brown, B., Clausing, K.J., Turner, V.S., Vainchtein, I.D., Molofsky, A.V., and Kheirbek, M.A. (2020). Circuit and molecular architecture of a ventral hippocampal network. Nat. Neurosci. *23*, 1444–1452.

Hao, J.X., Xu, I.S., Xu, X.J., and Wiesenfeld-Hallin, Z. (1999). Effects of intrathecal morphine, clonidine and baclofen on allodynia after partial sciatic nerve injury in the rat. Acta Anaesthesiol. Scand. *43*, 1027–1034.

Houser, C.R., Peng, Z., Wei, X., Huang, C.S., and Mody, I. (2021). Mossy cells in the dorsal and ventral dentate gyrus differ in their patterns of axonal projections. J. Neurosci. *41*, 991–1004.

Hsu, T.T., Lee, C.T., Tai, M.H., and Lien, C.C. (2016). Differential recruitment of dentate gyrus interneuron types by commissural versus perforant pathways. Cereb. Cortex *26*, 2715–2727.

Jimenez, J.C., Su, K., Goldberg, A.R., Luna, V.M., Biane, J.S., Ordek, G., Zhou, P., Ong, S.K., Wright, M.A., Zweifel, L., et al. (2018). Anxiety cells in a hippocampal-hypothalamic circuit. Neuron *97*, 670–683.e6.

Jin, J., and Maren, S. (2015). Fear renewal preferentially activates ventral hippocampal neurons projecting to both amygdala and prefrontal cortex in rats. Sci. Rep. *5*, 8388.

Jinde, S., Zsiros, V., Jiang, Z., Nakao, K., Pickel, J., Kohno, K., Belforte, J.E., and Nakazawa, K. (2012). Hilar mossy cell degeneration causes transient dentate granule cell hyperexcitability and impaired pattern separation. Neuron *76*, 1189–1200.

Jinno, S., Ishizuka, S., and Kosaka, T. (2003). Ionic currents underlying rhythmic bursting of ventral mossy cells in the developing mouse dentate gyrus. Eur. J. Neurosci. *17*, 1338–1354.

Jovanovic, T., and Ressler, K.J. (2010). How the neurocircuitry and genetics of fear inhibition may inform our understanding of PTSD. Am. J. Psychiatry *167*, 648–662.

Kheirbek, M.A., and Hen, R. (2011). Dorsal vs ventral hippocampal neurogenesis: implications for cognition and mood. Neuropsychopharmacology *36*, 373–374.

Kheirbek, M.A., Drew, L.J., Burghardt, N.S., Costantini, D.O., Tannenholz, L., Ahmari, S.E., Zeng, H., Fenton, A.A., and Hen, R. (2013). Differential control of learning and anxiety along the dorsoventral axis of the dentate gyrus. Neuron *77*, 955–968.

Khemka, S., Barnes, G., Dolan, R.J., and Bach, D.R. (2017). Dissecting the function of hippocampal oscillations in a human anxiety model. J. Neurosci. *37*, 6869–6876.

Kim, W.B., and Cho, J.H. (2017). Synaptic targeting of double-projecting ventral CA1 hippocampal neurons to the medial prefrontal cortex and basal amygdala. J. Neurosci. *37*, 4868–4882.

Kim, S.Y., Adhikari, A., Lee, S.Y., Marshel, J.H., Kim, C.K., Mallory, C.S., Lo, M., Pak, S., Mattis, J., Lim, B.K., et al. (2013). Diverging neural pathways assemble a behavioural state from separable features in anxiety. Nature *496*, 219–223.

Krashes, M.J., Koda, S., Ye, C., Rogan, S.C., Adams, A.C., Cusher, D.S., Maratos-Flier, E., Roth, B.L., and Lowell, B.B. (2011). Rapid, reversible activation of AgRP neurons drives feeding behavior in mice. J. Clin. Invest. *121*, 1424–1428.

Lee, C.T., Kao, M.H., Hou, W.H., Wei, Y.T., Chen, C.L., and Lien, C.C. (2016). Causal evidence for the role of specific GABAergic interneuron types in entorhinal recruitment of dentate granule cells. Sci. Rep. *6*, 36885.

Lee, A.T., Cunniff, M.M., See, J.Z., Wilke, S.A., Luongo, F.J., Ellwood, I.T., Ponnavolu, S., and Sohal, V.S. (2019). VIP interneurons contribute to avoidance behavior by regulating information flow across hippocampal-prefrontal networks. Neuron *102*, 1223–1234.e4.

Lisman, J.E. (1999). Relating hippocampal circuitry to function: recall of memory sequences by reciprocal dentate-CA3 interactions. Neuron *22*, 233–242.

Liu, Y.C., Cheng, J.K., and Lien, C.C. (2014a). Rapid dynamic changes of dendritic inhibition in the dentate gyrus by presynaptic activity patterns. J. Neurosci. *34*, 1344–1357.

Liu, Y.T., Shao, Y.W., Yen, C.T., and Shaw, F.Z. (2014b). Acid-induced hyperalgesia and anxio-depressive comorbidity in rats. Physiol. Behav. *131*, 105–110.

Lübke, J., Deller, T., and Frotscher, M. (1997). Septal innervation of mossy cells in the hilus of the rat dentate gyrus: an anterograde tracing and intracellular labeling study. Exp. Brain Res. *114*, 423–432.

Moretto, J.N., Duffy, Á.M., and Scharfman, H.E. (2017). Acute restraint stress decreases c-fos immunoreactivity in hilar mossy cells of the adult dentate gyrus. Brain Struct. Funct. *222*, 2405–2419.

Moser, M.B., Moser, E.I., Forrest, E., Andersen, P., and Morris, R.G. (1995). Spatial learning with a minislab in the dorsal hippocampus. Proc. Natl. Acad. Sci. USA *92*, 9697–9701.

O'Keefe, J., and Dostrovsky, J. (1971). The hippocampus as a spatial map. Preliminary evidence from unit activity in the freely-moving rat. Brain Res. *34*, 171–175.

Oh, S.J., Cheng, J., Jang, J.H., Arace, J., Jeong, M., Shin, C.H., Park, J., Jin, J., Greengard, P., and Oh, Y.S. (2020). Hippocampal mossy cell involvement in behavioral and neurogenic responses to chronic antidepressant treatment. Mol. Psychiatry *25*, 1215–1228.

Padilla-Coreano, N., Bolkan, S.S., Pierce, G.M., Blackman, D.R., Hardin, W.D., Garcia-Garcia, A.L., Spellman, T.J., and Gordon, J.A. (2016). Direct ventral hippocampal-prefrontal input is required for anxiety-related neural activity and behavior. Neuron *89*, 857–866.

Parfitt, G.M., Nguyen, R., Bang, J.Y., Aqrabawi, A.J., Tran, M.M., Seo, D.K., Richards, B.A., and Kim, J.C. (2017). Bidirectional control of anxiety-related behaviors in mice: role of inputs arising from the ventral hippocampus to the lateral septum and medial prefrontal cortex. Neuropsychopharmacology *42*, 1715–1728.

Patel, A., and Bulloch, K. (2003). Type II glucocorticoid receptor immunoreactivity in the mossy cells of the rat and the mouse hippocampus. Hippocampus *13*, 59–66.

Pellow, S., Chopin, P., File, S.E., and Briley, M. (1985). Validation of open:-closed arm entries in an elevated plus-maze as a measure of anxiety in the rat. J. Neurosci. Methods *14*, 149–167.

Pinault, D. (1996). A novel single-cell staining procedure performed in vivo under electrophysiological control: morpho-functional features of juxtacellularly labeled thalamic cells and other central neurons with biocytin or Neurobiotin. J. Neurosci. Methods *65*, 113–136.

Scharfman, H.E. (1995). Electrophysiological evidence that dentate hilar mossy cells are excitatory and innervate both granule cells and interneurons. J. Neurophysiol. *74*, 179–194.

Scharfman, H.E. (2016). The enigmatic mossy cell of the dentate gyrus. Nat. Rev. Neurosci. *17*, 562–575.

Scharfman, H.E., and Myers, C.E. (2013). Hilar mossy cells of the dentate gyrus: a historical perspective. Front. Neural Circuits *6*, 106.

Schoenfeld, T.J., Rada, P., Pieruzzini, P.R., Hsueh, B., and Gould, E. (2013). Physical exercise prevents stress-induced activation of granule neurons and enhances local inhibitory mechanisms in the dentate gyrus. J. Neurosci. *33*, 7770–7777.

Sengupta, A., Yau, J.O.Y., Jean-Richard-Dit-Bressel, P., Liu, Y., Millan, E.Z., Power, J.M., and McNally, G.P. (2018). Basolateral amygdala neurons maintain aversive emotional salience. J. Neurosci. *38*, 3001–3012.

Sharma, N.K., Ryals, J.M., Liu, H., Liu, W., and Wright, D.E. (2009). Acidic saline-induced primary and secondary mechanical hyperalgesia in mice. J. Pain *10*, 1231–1241.

Sluka, K.A., Kalra, A., and Moore, S.A. (2001). Unilateral intramuscular injections of acidic saline produce a bilateral, long-lasting hyperalgesia. Muscle Nerve *24*, 37–46.

Squire, L.R. (2009). Memory and brain systems: 1969-2009. J. Neurosci. *29*, 12711–12716.

Sternson, S.M., and Roth, B.L. (2014). Chemogenetic tools to interrogate brain functions. Annu. Rev. Neurosci. *37*, 387–407.

Sun, Y., Grieco, S.F., Holmes, T.C., and Xu, X. (2017). Local and long-range circuit connections to hilar mossy cells in the dentate gyrus. eNeuro *4*, ENEURO.0097-17.2017.

Tanaka, K.F., Samuels, B.A., and Hen, R. (2012). Serotonin receptor expression along the dorsal-ventral axis of mouse hippocampus. Philos. Trans. R. Soc. Lond. B Biol. Sci. *367*, 2395–2401.

Thieme, K., Turk, D.C., and Flor, H. (2004). Comorbid depression and anxiety in fibromyalgia syndrome: relationship to somatic and psychosocial variables. Psychosom. Med. *66*, 837–844.

Weeden, C.S., Roberts, J.M., Kamm, A.M., and Kesner, R.P. (2015). The role of the ventral dentate gyrus in anxiety-based behaviors. Neurobiol. Learn. Mem. *118*, 143–149.

Williams, P.A., Larimer, P., Gao, Y., and Strowbridge, B.W. (2007). Semilunar granule cells: glutamatergic neurons in the rat dentate gyrus with axon collaterals in the inner molecular layer. J. Neurosci. *27*, 13756–13761.

Zou, D., Chen, L., Deng, D., Jiang, D., Dong, F., McSweeney, C., Zhou, Y., Liu, L., Chen, G., Wu, Y., and Mao, Y. (2016). DREADD in parvalbumin interneurons of the dentate gyrus modulates anxiety, social interaction and memory extinction. Curr. Mol. Med. *16*, 91–102.

Zucca, S., Griguoli, M., Malézieux, M., Grosjean, N., Carta, M., and Mulle, C. (2017). Control of spike transfer at hippocampal mossy fiber synapses in vivo by $GABA_A$ and $GABA_B$ receptor-mediated inhibition. J. Neurosci. *37*, 587–598.

STAR★METHODS

KEY RESOURCES TABLE

REAGENT or RESOURCE	SOURCE	IDENTIFIER
Antibodies		
rabbit anti-GluR2/3	Merck Millipore	Millipore Cat# AB1506; RRID: AB_90710
rabbit anti-RFP pre-adsorbed	Rockland	Rockland Cat# 600-401-379S; RRID: AB_11182807
Alexa Fluor 594 goat anti-rabbit	Thermo Fisher Scientific	Thermo Fisher Scientific Cat# A-11012; RRID: AB_2534079
Alexa Fluor 633 goat anti-rabbit	Thermo Fisher Scientific	Thermo Fisher Scientific Cat# A-21070; RRID: AB_2535731
Alexa Fluor 488-streptavidin	Thermo Fisher Scientific	Thermo Fisher Scientific Cat# S11223
Alexa Fluor 594-streptavidin	Thermo Fisher Scientific	Thermo Fisher Scientific Cat# S11227
Bacterial and virus strains		
AAV1-Syn-Flex-GCaMP6s-WPRE-SV40	Chen et al., 2013	Addgene viral prep# 100845-AAV1
AAV5-Syn-Flex-GCaMP6s-WPRE-SV40	Chen et al., 2013	Addgene viral prep# 100845-AAV5
AAV5-hSyn-DIO-hM3D(Gq)-mCherry	Krashes et al., 2011	Addgene viral prep# 44361-AAV5
AAV5-hSyn-DIO-hM4D(Gi)-mCherry	Krashes et al., 2011	Addgene viral prep# 44362-AAV5
AAV5-hSyn-DIO-mCherry	A gift from Bryan Roth, University of North Carolina	Addgene viral prep# 50459-AAV5
AAV5-EF1α-DIO-hChR2(H134R)-eYFP	University of North Carolina vector core	# AAV5-EF1α-DIO-hChR2(H134R)-eYFP
AAV5-EF1α-DIO-eYFP	University of North Carolina vector core	# AAV5-EF1α-DIO-eYFP
AAV5-EF1α-DIO-eNpHR3.0-eYFP	University of North Carolina vector core	# AAV5-EF1α-DIO-eNpHR3.0-eYFP
Chemicals, peptides, and recombinant proteins		
Clozapine N-oxide	Sigma-Aldrich	Cat# C0832
Dimethyl sulfoxide	J.T.Baker	Cat# 9224-06
Kynurenic acid	Sigma-Aldrich	Cat# K3375
SR95531	Abcam	Cat# ab120042
Paraformaldehyde	Sigma-Aldrich	Cat# 158127
Biocytin	Invitrogen	Cat# B-1592
Neurobiotin	Vector Laboratories	Cat# sp-1120
Experimental models: organisms/strains		
C57BL/6N Tg(Calcrl,cre)4688Nkza/J	Dr. Kazu Nakazawa's lab, University of Alabama at Birmingham	RRID: IMSR_JAX:023014
C57BL/6JNarl	National Laboratory Animal Center (Taiwan)	Stock# RMRC11005
Software and algorithms		
EthoVison XT13 software	Noldus	https://www.noldus.com
SMART 3.0 video tracking software	Panlab	https://www.panlab.com/en/products/smart-video-tracking-software-panlab
Doric Neuroscience Studio V5.3.3	Doric	https://doriclenses.com
GraphPad Prism 6	GraphPad	https://www.graphpad.com
pClamp and Clampfit 10.3	Molecular Devices	https://www.moleculardevices.com
Python	Jupyter notebook	https://jupyter.org
Neuromantic 1.6.3	University of Reading	https://www.reading.ac.uk/neuromantic/body_index.php
HBP Neuron Morphology Viewer	NeuroInformatics.NL	https://neuroinformatics.nl/HBP/morphology-viewer/

(*Continued on next page*)

Continued

REAGENT or RESOURCE	SOURCE	IDENTIFIER
ImageJ	ImageJ	https://imagej.net
Coreldarw X8	CorelDRAW	https://www.coreldraw.com/en/
Other		
1-site Fiber Photometry System	Doric	Cat# FPS_1S_405/GFP_400-0.57
Metal Fiber Optic Cannula	Inper	Cat# FOC-M-400-1.25-0.50-5.0
Fiberoptic Rotary Joint	Doric	Cat# FRJ_1x1_FC-FC
Optical Fiber	Thorlabs	Cat# FT200UMT
Multimode Ceramic Zirconia Ferrules	Precision Fiber Products	Cat# 165254857
589 nm DPSS Laser System	OEM Laser	Cat# MLG-F-589-50mW
The microsyringe pump	Kd Scientific	Cat# KDS310
NanoFil 10 μL syringe	World Precision Instruments	Cat# NANOFIL
34G beveled NanoFil needle	World Precision Instruments	Cat# NF34BV-2
Microtome	Leica	Cat# SM2010R
Microslicers	Dosaka	Cat# DTK-1000
ELC Amplifier	npi electronic	Cat# ELC-01MX
MultiClamp 700B Microelectrode Amplifier	Molecular Devices	Cat# MULTICLAMP 700B
Digitizer	Molecular Devices	Cat# Digidata 1440A
Single-Barrel Borosilicate Capillary Glass with Microfilament	A-M system	Cat# 602000
Borosilicate Glass with Filament	Harvard Apparatus	Cat# GC150F-7.5

RESOURCE AVAILABILITY

Lead contact

Further information and requests for resources and reagents should be directed to and will be fulfilled by the Lead Contact, Cheng-Chang Lien (cclien@nycu.edu.tw).

Materials availability

This study did not generate any unique reagents.

Data and code availability

- All data reported in this paper will be shared by the lead contact upon request.
- This paper does not report original code.
- Any additional information required to reanalyze the data reported in this paper is available from the lead contact upon request.

EXPERIMENTAL MODEL AND SUBJECT DETAILS

Animal model

Crlr-Cre mice (also known as C57BL/6N-Tg(Calcrl,cre)4688Nkza/J) were obtained from Dr. Kazu Nakazawa (Jinde et al., 2012). C57BL/6J mice were obtained from Taiwan National Laboratory Animal Center. Both male and female mice (3–8 months old) were used in the behavioral and electrophysiological studies. All mice were bred on a C57BL/6J background. Mice were housed in a reverse 12-h light-dark cycle and were provided food and water *ad libitum*. Animals were handled in accordance with the national and institutional guidelines. All experimental protocols were approved by the Animal Care and Use Committee of the National Yang Ming Chiao Tung University.

Fibromyalgia model

To establish the FM model, we followed the induction protocol described previously (Sharma et al., 2009; Sluka et al., 2001). Two injections of acidic saline (20 μL/injection) were administered to the left gastrocnemius muscle on day 0 (baseline, [BL]) and on day 3. The acidic saline containing 0.01 M 2-(N-Morpholino) ethanesulfonic acid was adjusted to pH 4.0. The pH value of normal saline for sham group is 7.2.

METHOD DETAILS

Viruses

In the chemogenetic experiment, we virally expressed excitatory or inhibitory designer receptors exclusively activated by designer drugs (eDREADDs or iDREADDs) on MCs specifically by injecting the rAAV5-hSyn-DIO-hM3D(Gq)-mCherry (7.8×10^{12} vector genomes/mL; Addgene, Watertown, MA, USA) or rAAV5-hSyn-DIO-hM4D(Gi)-mCherry (4.7×10^{12} vector genomes/mL; Addgene) into the DG of *Crlr-Cre*$^{+/-}$ mice. In the control experiment, AAV5-hSyn-DIO-mCherry (4×10^{12} vector genomes/mL; Addgene) and AAV5-EF1α-DIO-eYFP (4.0×10^{12} vector genomes/mL, UNC) were used. In the fiber photometry experiment, the AAV1-Syn-Flex-GCaMP6s-WPRE-SV40 (2.9×10^{13} vector genomes/mL, Addgene) or AAV5-Syn-Flex-GCaMP6s-WPRE-SV40 (1.1×10^{13} vector genomes/mL, Addgene) was used. In the optogenetic experiment, the AAV5-EF1α-DIO-hChR2(H134R)-eYFP (ChR2, 4.3×10^{12} vector genomes/mL, University of North Carolina, Chapel Hill, NC, USA) and AAV5-EF1α-DIO-eNPHR3.0-eYFP (NpHR, 4.0×10^{12} vector genomes/mL, UNC) were used.

Stereotaxic injection

Mice (postnatal day > 56) were anesthetized with 4% isoflurane (vol/vol; Halocarbon Laboratories, North Augusta, SC, USA) in a 100% oxygen-containing induction chamber, and their heads were shaved for further operation. Mice were placed in a stereotaxic frame (IVM-3000, Scientifica, Uckfield, UK). The faces of the mice were covered by anesthetizing masks, supplied with approximately 1.5% isoflurane (airflow, 4 mL/min). A homeothermic pad (Physitemp Instruments, Clifton, NJ, USA, or TMP-5b, Supertech Instruments, Budapest, Hungary) was placed below the mice to maintain a constant body temperature (34–36°C). After securing the head with ear bars, 75% ethanol was used to sterilize the surgical area, and the eyes were protected using ophthalmic gel. A midline scalp incision (1 cm) was made with scissors and the skin was pulled aside to expose the skull. To target hilar MCs in either the dorsal or ventral HPC, a small craniotomy was made directly above the dorsal (AP: −1.7 mm, ML: ± 1.0 mm, DV: −2.0 and −1.8 mm) or ventral DG (AP: −3.5 mm, ML: ± 2.8 mm, DV: −3.0 and −2.8 mm). The viruses were delivered through the craniotomy to the locations within the dorsal or ventral DG, using a 10 μL NanoFil syringe (World Precision Instruments, Sarasota, FL, USA) and a 34-G beveled metal needle. Injection volume (0.15 μL at each location) and flow rate (0.1 μL/min) were controlled with a nanopump controller (KD Scientific, Holliston, MA, USA). After viral injection, the needle was raised 0.1 mm above the injection sites for an additional 10 min and then slowly withdrawn to minimize the upward flow of the viral solution. After withdrawing the needle, the incision was closed by suturing, and the mice were returned to their home cage for recovery. To reduce postoperative pain, ketorolac (6 mg/kg, i.p.) or carprofen (5 mg/kg, s.c.) was administered. All animals were allowed to rest for at least 3–4 weeks before the behavioral and electrophysiological experiments.

Fiber optic implantation

To allow the expression of viruses, optical fiber implantation was performed 3−4 weeks after viral injection. In fiber photometry experiments, a fiber-optic cannula (fiber core, 400 μm; 0.5 NA; 5 mm length; FOC-M-400-1.25-0.50-5.0; Inper, Hangzhou, Zhejiang, China) was implanted approximately 0.1 mm above the injection site and fixed with dental cement and Super-Bond C&B (Sun Medical, Shiga, Japan) to the skull. In optogenetic experiments, the fiber-optic cannula which consisted of a ferrule (1.25-mm diameter and 6.4-mm length; Precision Fiber Products, Milpitas, CA, USA) and an optical fiber with a flat tip (230-μm diameter) was implanted in the bilateral ventral DG at the following coordinates: (AP: −3.5 mm, ML: ± 2.8 mm, DV: −2.5 or −2.6 mm), and fixed with dental cement and Super-Bond C&B.

In vivo fiber photometry

After recovery from optical fiber implantation for 5–7 days, the mice were handled by the experimenter for 3–5 days and were habituated to the fiber optic connection for 3–5 days. After habituation, mice were placed in the behavioral apparatus and joined to a fiber photometry cannula holder for the measurement of calcium signals. Calcium signals were detected using an optical fiber photometry setup (Figure 1C left, Doric Lenses, Quebec City, Quebec, Canada). Two excitation wavelengths, 405 and 465 nm, were used in this system. The 405-nm wavelength (isosbestic point), which excited the auto-fluorescence, was reflected by the first dichroic mirror and passed through the second dichroic mirror in a mini-cube (FMC4, Doric Lenses). The 465-nm wavelength, which excited the calcium-dependent GCaMP fluorescence, passed through both the first and second dichroic mirrors. The emission wavelengths (500–550 nm) from the activated GCaMP fluorescence and autofluorescence, were reflected by the second dichroic mirror and sent to the detector port based on the different detection frequencies of two excitation wavelengths. The fluorescence signals were then transmitted to a fluorescence detector amplifier for signal amplification. The acquired data were further transformed into normalized ΔF (ΔF/F%) using the Doric Neuroscience Studio software. The ΔF/F% represented the percentage of fluorescence change, calculated as $100\% \times (F_{465}(t) - F_{405}(t))/F_{405}(t)$ (Sengupta et al., 2018), where F_{405} indicated the baseline fluorescence excited by 405-nm light; F_{465} indicated the calcium-dependent GCaMP fluorescence excited by 465-nm light and the t represented the time. Experiments with either AAV1 or AAV5 yielded similar results (Figures S2A and S2B) and were therefore pooled.

Behavioral tests

After a 3-week recovery from surgery, mice were housed singly for at least 1 week (except for the acid-induced chronic pain model). All mice used in the chemogenetic behavioral experiments were handled by an experimenter for 5–7 days before the behavioral tests.

In fiber photometry and optogenetic experiments, mice were handled for 3–5 days, followed by optical tether habituation in the home cage for 3 days. All behavioral tests were conducted during the light period of each cycle. Mice were moved to the behavioral room with dim light for at least 30 min before either drug delivery or fiber-optic patch cord connection for habituation. In chemogenetic experiments, mice expressing DREADD receptors or mCherry fluorescent protein were intraperitoneally injected with clozapine N-oxide (CNO, 5 mg/kg, Sigma-Aldrich, St Louis, MO, USA) 40–50 min before the test session. The procedures of each behavioral test were as follows:

(1) *Elevated plus maze (EPM) and elevated zero maze (EZM) tests*: The apparatus was made of white acrylic plastic with a plus or zero shape. The plus shape of EPM consisted of two open arms (30 × 5 cm) and two closed arms (30 × 5 × 25 cm) extending from the intersection zone (5 × 5 cm). The EZM was composed of two open areas and two closed areas. The outer diameter of the EZM was 50 cm. The track width was 5 cm, and the wall height of the closed arm was 25 cm. Both EPM and EZM were elevated 50 cm above the floor. In the chemogenetic experiments, mice were allowed to freely explore in the EPM for 10 min. In fiber photometry experiments, mice freely explored the EPM and EZM for 10–15 min. In some experiments, mice spent an additional 10 min in a modified EPM with three open arms after exploring for 10–15 min in the normal EPM. In optogenetic experiments, mice freely explored the EZM for 15 min, and received alternating optogenetic stimulation (constant 589 nm laser light, 6-10 mW, OEM Laser System, Midvale, UT, USA) for 3 min. The 589 nm light was delivered in the second and fourth epochs. For the closed-loop NpHR silencing experiment in EPM, mice received the laser once located in the center and the open arms of the EPM. Real-time video tracking and laser triggering was achieved using a SMART video tracking system (Panlab, Barcelona, Spain). The recorded videos were analyzed by video tracking system at a frame rate of 29 frames per second (EthoVision, Noldus, Wageningen, Netherlands). The heatmaps shown in Figures 1D and 1K represented the relative time spent by each mouse in the arena of the EPM and EZM and were plotted by EthoVision software. The apparatus was wiped with 75% ethanol after each trial. The data were excluded if the optical tether was twisted or stuck to the walls of the EZM and EPM. In closed-loop EPM tests, data were excluded if the real-time detection system did not detect the mouse's location precisely.

(2) *Open field test (OFT)*: The OFT was performed in a transparent and square open-field chamber (24 × 24 cm^2, Coulbourn Instruments, Holliston, MA, USA). The center zone was defined as 15 × 15 cm at the center of the arena, and the rest of the region of the arena was defined as the margin zone. Mice were placed at the center of the arena at the beginning and were then allowed to explore freely for 15 min. The exploratory activity of the mice was detected by infrared beams equipped in the open field chamber. The hardware detected beams broken when the mice went through. Therefore, the traveling tracks and locations of mice can be determined by connecting the broken-point of infrared beams. The total travel distance indicated the locomotion activity of the mice. The percentage of time spent in the center zone represented the anxiety index of the mouse model. The chamber was cleaned with 75% ethanol after each trial to avoid odor cues.

(3) *Marble-burying test*: Mice were individually placed into cages (12.5 × 28 × 13 cm) filled with 6-cm-deep clean bedding. Twenty-four glass marbles (1.5-cm diameter) were spaced 4 cm apart on the surface of the bedding. Mice were initially placed at the corner of the marble-containing cage and then left for 30 min. Marbles, which were more than two-thirds of their volume covered by the bedding, were defined as buried marbles. In optogenetic experiments, the test session was composed of four alternating light ON and OFF epochs, with a constant 589 nm laser beam (6-10 mW) delivered in the first and third epochs (light ON, OFF, ON, OFF) (Lee et al., 2019). Each epoch was 5 min long and the test session lasted for 20 min. To prevent the mice from escaping from the experimental cage, 25-cm plastic walls were placed above the edge of cage to extend the height of the walls.

(4) *Von Frey test*: Von Frey filaments were used to test the mechanical hyperalgesia of mice before and after pain induction. Mice were subjected to an elevated apparatus with fencing. Different filaments were applied through the floor mesh to the plantar surface of both hind paws. The mechanical sensitivity of each foot was quantified by the diameter of the thickest filament that triggered the withdrawal behavior more than three times in five stimulations (Blackburn-Munro and Jensen, 2003; Hao et al., 1999).

In vivo juxtacellular recording

Mice were anesthetized with 4% isoflurane during the induction period. The mice were placed onto the stereotaxic frame and anesthetized with 1%–1.5% isoflurane in 100% oxygen-containing airflow. The body temperature was maintained using a heating pad (TMP-5b, Supertech Instruments, Budapest, Hungary). To implant the recording electrode, craniotomies were performed above the DG and CA1 (dorsal, AP, −1.5 to −2.0 mm; ML, ± 0.8 to 1.3 mm; ventral, AP, −3.2 to −3.5 mm; ML, 2.4 to 2.8 mm for DG; ML, 3.3 to 3.6 mm for CA1). An optical fiber (200-μm diameter) with a ferrule (1.25-mm diameter and 6.4-mm length) was positioned 70° to the surface and placed at the following coordinates: AP, −1.7 mm; ML, 1.5 mm and DV, 1.7 mm for the dorsal DG and AP, −3.5 mm; ML, 3.3 mm and DV, 2.0 mm for the ventral DG. Activation of ChR2-expressing MCs was achieved by delivering blue light through a 473-nm laser (OEM Laser Systems, Midvale, UT, USA) with 35-mW light intensity (Zucca et al., 2017). For juxtacellular recording of neuronal firing, a single-barrel borosilicate capillary glass electrode (outer diameter, 1.2 mm; inner diameter, 0.68 mm; A-M system, Carlsborg, WA, USA) was filled with 1.5%–2% Neurobiotin (SP-1120, Vector Laboratories, Burlin-game, CA, USA) in 0.5 M NaCl. The pipette impedance was between 5 and 12 MΩ. Juxtacellular labeling was performed by injecting an

anodal current pulse (0.5–10.0 nA, 200 ms) as previously described (Pinault, 1996). To monitor the sleeping state of mice under anesthesia, a pipette for local field potential recording was placed onto the layer I of the cortex filled with 0.5 M NaCl. Signals from the pre-amplification headstage were amplified 1000-fold, and high-pass filtered at 1 Hz (ELC01-MX, NPI Electronic, Tamm, Germany). Signals were band-pass filtered at 1 Hz to 5 kHz and sampled at 40 kHz by a digitizer (Digidata 1440A, Molecular Devices, San Jose, CA, USA). Spikes were band-pass filtered at 300 Hz–5 kHz during signals acquisition (DPA-2FS, NPI Electronic).

Slice preparation and patch-clamp recording

After at least 3 weeks of recovery from surgery or all behavioral tests, virus-injected mice were sacrificed by rapid decapitation. Acute coronal or horizontal brain slices of 300-μm thickness were cut using a vibratome (DTK-1000; Dosaka, Kyoto, Japan) using ice-cold sucrose saline containing (in mM) 87 NaCl, 25 $NaHCO_3$, 1.25 NaH_2PO_4, 2.5 KCl, 10 glucose, 75 sucrose, 0.5 $CaCl_2$, and 7 $MgCl_2$. Slices were recovered in oxygenated (95% O_2 and 5% CO_2) sucrose saline containing chamber at 34°C for 30 min and were then kept at room temperature until use. During the experiment, slices were transferred to a submerged chamber and perfused with oxygenated artificial cerebrospinal fluid (ACSF) containing (in mM): 125 NaCl, 25 $NaHCO_3$, 1.25 NaH_2PO_4, 2.5 KCl, 25 glucose, 2 $CaCl_2$, and 1 $MgCl_2$, at room temperature. The mCherry or eYFP expression was confirmed by red or green fluorescence and neurons in the DG were visually selected for recordings under an infrared differential interference contrast microscope (BX51WI, Olympus, Tokyo, Japan). For optical stimulation, ChR2-expressing and NpHR-expressing neurons were respectively excited by 470-nm and 590-nm LED light (driven by DC4104, Thorlabs, Newton, NJ, USA), which were delivered directly through the objective.

Whole-cell patch-clamp recordings were made using an Axopatch 200B amplifier or Multiclamp 700B amplifier (Molecular Devices, San Jose, CA, USA). Recording electrodes (3–7 MΩ) were pulled from borosilicate glasses (outer diameter, 1.5 mm; 0.32 mm wall thickness; Harvard Apparatus, Holliston, MA, USA) and filled with a low Cl^- internal solution containing (in mM): 136.8 K-gluconate, 7.2 KCl, 0.2 EGTA, 4 MgATP, 10 HEPES, 7 Na_2-phosphocreatine, 0.5 Na_3GTP (pH 7.3 with KOH), and 0.4% biocytin (wt/vol, Thermo Fisher Scientific, Waltham, MA, USA). The pipette capacitance was compensated in the cell-attached mode. For most of the recordings, the series resistance was compensated to 70%–80% in the voltage-clamp configuration and 100% in the current-clamp configuration. Signals were low-pass filtered at 4 kHz (four-pole Bessel filter) and sampled at 10 kHz using a digitizer (Digidata 1440A). Pulse sequences were generated using a digitizer (Digidata 1440A) and pCLAMP 10.3 software (Molecular Devices).

Solutions and drugs

In the behavioral tests, CNO was dissolved in 0.9% NaCl with 10% dimethyl sulfoxide (DMSO). The Veh control also contained 10% DMSO in 0.9% NaCl solution. In the *ex vivo* slice recording, the following antagonists were added to the ACSF: 2 mM kynurenic acid (Sigma-Aldrich) to block AMPA and NMDA receptors and 1 μM gabazine (Abcam, Cambridge, UK) to block $GABA_A$ receptors. To activate DREADD receptors, 5 μM CNO was superfused to the bath.

Immunohistochemistry and histology

To identify the biocytin-filled neurons, brain slices were fixed overnight with 4% paraformaldehyde (PFA; w/v) in phosphate-buffered saline (PBS). After washing three times with PBS, slices were soaked in 0.3% Triton X-100 (vol/vol; USB Co., Cleveland, OH, USA) for 30 min. The slices were then incubated with streptavidin-conjugated Alexa Fluor 488 or 594 (1:400; Thermo Fisher Scientific) in PBS containing 0.3% Triton X-100 and 2% normal goat serum (NGS, Vector Laboratories, Burlin-game, CA, USA) at 4°C overnight. After washing six times with PBS, slices were mounted onto slides using Vectashield mounting medium containing 4′,6-diamidino-2-phenylindole (DAPI, H-1200, Vector Laboratories, Burlin-game, CA, USA).

For samples collected from the cryosections, mice were perfused with ice-cold PBS, followed by 4% PFA using the transcardial procedure. The fixed brains were removed and post-fixed in 4% PFA for an additional 6 h or overnight. After dehydration with 15% sucrose for 4 h, followed by 30% sucrose in PBS for 24 h, the fixed brains were sliced into 50-μm coronal slices using a microtome (SM2010R, Leica Microsystems, Buffalo Grove, IL, USA). Collected brain slices were washed with PBS and blocked with 0.3% Triton X-100 for 30 min and 10% NGS for 2 h in PBS. The slices were then incubated overnight with 0.3% Triton X-100 and 5% NGS with a primary antibody: GluR2/3 (1:200, AB1506, Millipore, Burlington, MA, USA) or anti-red fluorescent protein (1:300, rabbit monoclonal, 600-401-379S, Rockland, Limerick, PA, USA) at 4°C. After washing three times with PBS, the slices were incubated with secondary antibodies against rabbit immonoglobulins for 2 h at room temperature. After washing six times with PBS, the slices were mounted onto slides with DAPI-containing mounting medium.

To label the Neurobiotin-filled cells after juxtacellular recordings, mice were transcardially perfused as described above, and 60-μm slices were collected. After washing, slices were incubated in streptavidin-conjugated Alexa Fluor 594 (1:1000; Thermo Fisher Scientific) with 2% NGS in TBS containing 0.1% Triton X-100 at 4°C overnight or at room temperature for 2 h. Then, the stained brain slices were scanned using a confocal/two-photon laser excitation microscope (Leica SP5 module, Leica Microsystems). Confocal image stacks of labeled cells were reconstructed using Neuromantic 1.6.3 software (developed by Darren Myatt, University of Reading, Berkshire, UK).

QUANTIFICATION AND STATISTICAL ANALYSIS

Electrophysiological data were analyzed using Clampfit 10.3 (Molecular Devices), or a custom-made program written in Python. In order to classify the juxtacellularly recorded neurons, the spike half-width, which was defined as the duration of the waveform above 50% of the peak spike amplitude relative to the baseline, was calculated for each spike. Neurons with averaged spike half-width < 0.4 ms were defined as putative INs; otherwise, they were putative GCs. For fiber photometry, we first matched the time points of Ca^{2+} signals with behavioral time points, then averaged the 200 sample points (100 sample points before and 100 sample points after the corresponding time points) of Ca^{2+} signals for matched time points. To show the dependency of the Ca^{2+} signals on the mouse locations in the EPM or EZM, the trajectory of mouse was spatially binned by 0.35 × 0.35 cm^2 pixel areas, and the Ca^{2+} signals were averaged within each pixel in the whole experimental session (Figures 1F and 1M). To correlate the variations of the Ca^{2+} signals with different types of arm transitions, unidirectional segments of the trajectories crossing the maze center and longer than 30 cm were identified as qualified transitions in the EPM. The transitions were further categorized based on their starts and ends, that is, transitions from an open arm to a closed arm (O→C), C→O, C→C, and O→O (Figure 1G). For EZM, mouse locations were further converted into degrees, and the transition points were set at 45°, 135°, 225° and 315°. The trajectories crossing the transition points, and encompassing more than 90 degrees were selected and the Ca^{2+} signals at corresponding degrees were shown as color-coded stripes (Figure 1N). The extracted segments of the trajectories in Figure 1N are labeled in degrees relative to the transition points. To compare the distributions of the MC activity between the open and closed areas, the normalized Ca^{2+} signals (ΔF/F%) were first normalized to *z*-scores for each mouse. Then, the minimum and maximum values of the *z*-scores for all mice were determined and used as the full range for binning. The same 250 bins of an equal size [(max_*z*-score - min_*z*-score)/250] were used for the binning of all the probability distributions. The probability distributions of the *z*-scores from the open and closed areas were constructed separately. For each area and at each bin, the means and standard deviations of the corresponding *z*-score proportions were calculated across all mice (Figures 1H and 1O).

Statistical significance was tested using the Wilcoxon-signed rank test and Mann-Whitney test at the indicated significance level (p), or the two-way ANOVA with the Bonferroni test at the indicated significance level (α), using Prism 6.0 (GraphPad Software, La Jolla, CA, USA).